Bidirectional AC-DC Converter for Vehicle-to-Grid (V2G) Applications

Arjun Raj Prabu Andhra Sridhar
Marquette University

BI-DIRECTIONAL AC-DC CONVERTER FOR VEHICLE-TO-GRID (V2G) APPLICATIONS

by

Arjun Raj Prabu Andhra Sridhar

A Thesis submitted to the Faculty of the Graduate School,
Marquette University,
in Partial Fulfillment of the Requirements for
the Degree of Master of Science

Milwaukee, Wisconsin

December 2015

To my ever-supporting parents and my family

ABSTRACT
BI-DIRECTIONAL AC-DC CONVERTER
FOR VEHICLE-TO-GRID (V2G) APPLICATIONS

Arjun Raj Prabu Andhra Sridhar

Marquette University, 2015

Electric vehicles are growing at a rapid pace in the internal combustion engine dominated transportation sector, and bring environmental and economic benefits to society. Electric vehicles produce nearly zero carbon emission, provided that they are charged through renewable energy sources. Electric vehicles reduce our dependency on foreign oil and also offer additional benefits like Vehicle-to-grid (V2G). V2G is a technology that allows electric energy stored in the electric vehicle batteries to be returned to the grid during peak demand. V2G can also provide voltage regulation, voltage shaving, reactive power compensation and distributed generation. This necessitates that an electric vehicle battery charger be bi-directional, capable of sinking or sourcing real and reactive power. The state of the art battery charging converter is unidirectional and has multiple stages of power conversion.

In this thesis, a single phase, single stage, isolated, bi-directional Silicon Carbide (SiC) AC-DC converter based on Dual Active Bridge (DAB) topology is proposed and analyzed. Direct-quadrature axis (DQ) current control of the DAB-based topology is implemented with phase shift modulation. Simulation results are presented with various operating conditions showing the converter's ability to sink or source real and reactive power in the AC grid. Hardware and firmware implementation of a single phase bi-directional AC-DC converter operating at 100 kHz utilizing Silicon Carbide (SiC) MOSFETs are discussed in detail. Experimental results are shown confirming simulation results.

A single phase bi-directional AC-DC converter uses large electrolytic capacitors to filter ripple currents in the DC bus. Electrolytic capacitors are bulky and are prone to failure. These electrolytic capacitors can be eliminated by rejecting the ripple current in the DC bus. The ripple current is rejected by injecting a current of same magnitude and opposite phase to the ripple current. A rigorous analysis is performed on the ripple rejection technique used in single phase bi-directional AC-DC converters. Simulation results are presented to verify the analysis.

A three phase bi-directional AC-DC converter improves the charging time of the electric vehicles by charging the batteries at a higher power level. A three phase, single stage, isolated, bi-directional AC-DC converter is analyzed. DQ current control of the three phase AC-DC converter is implemented in simulation to verify the analysis.

ACKNOWLEDGMENTS

Arjun Raj Prabu Andhra Sridhar

My thesis work would not have been possible without the support from my advisor, committee members, family members and friends.

First, I would like to express my deepest gratitude to my advisor, Dr. Nathan Weise, for providing me support and guidance throughout my master's program. I gained valuable insights through his classes and discussions. He is a constant driving force of motivation to help me achieve my goals. I would like to thank Dr. Nabeel Demerdash for sharing his knowledge through his classes and making valuable suggestions and corrections to my thesis work. I would also like to thank Dr. Edwin Yaz for his suggestions to my thesis work.

I would also like to thank Lance Doiron for helping me with the hardware setup at the University of Maine. I would like to thank my fellow graduate students Jiangbiao He, Alireza Fatemi, Chad Somogyi at Marquette University and Asa Sproul at University of Maine for their suggestions and discussions.

I would like to thank my mother, my father and my sister for constantly supporting me while I work to achieve my goals and sending their best wishes from India and Oman. I would like to also thank my friends and well-wishers in the USA and also in India for their wholehearted support.

Finally, I want to thank the Department of Electrical and Computer Engineering at Marquette University and at University of Maine for financially supporting my master's thesis.

CONTENTS

LIST OF TABLES

LIST OF FIGURES

CHAPTER 1

INTRODUCTION

1.1 Background

Electrification of transportation vehicles has many significant benefits economically and environmentally. Electric vehicles (EV) or Plugin Hybrid Electric Vehicles (PHEV) have become popular in the past decade due to their high fuel economy and reduced carbon emission. The only emission produced due to the usage of EVs are from generating electricity to charge the EV battery pack. This emission is significantly smaller compared to the emission produced by gasoline powered engines.

Electric vehicles (EV) use electric motors for traction purposes and are powered solely by battery packs. Battery packs can be charged in any public charging station or home charging station. Electric vehicles are more suitable for city driving conditions where batteries can be charged easily using an electric outlet. They are not preferred for long distance driving, due to insufficient charging infrastructure and present battery technology.

Hybrid Electric Vehicles (HEV) are driven by electric motors and Internal Combustion Engines (ICE). The ICE is powered by petroleum and the electric motors are powered by battery packs. The battery packs can be charged by the electric motor during regenerative braking and also through the ICE during motoring. These battery packs cannot be charged using an electric outlet. A hybrid car switches between the electric motor and the ICE based on the driving condition in order to reduce fuel consumption. Hybrid cars are suitable for city driving conditions and also for long distance driving conditions.

Plug-in Hybrid Electric Vehicles (PHEV) are driven by electric motors accompanied by Internal Combustion Engines (ICE). The ICEs are powered by petroleum and the electric motors are powered by battery packs. The battery packs can be charged during regenerative braking, through the ICEs, and additionally by using an electric outlet. PHEVs give the best fuel economy and is dependent on how often the battery packs are charged using an electric outlet.

Another competitor to battery operated electric vehicles are hydrogen powered electric vehicles called the Fuel Cell Electric vehicle (FCEV). FCEVs use oxygen from the air and compressed hydrogen to generate electric power to drive the electric motors. It has been found that FCEVs are 12 times more expensive than conventional gasoline powered vehicles to operate [1].

1.2 Problem statement

Electrical energy stored in the electric vehicle battery is unused while it is parked. The stored electric energy in the battery can be returned back to the grid for purposes of supplying power during peak load, voltage regulation, reactive power compensation and distributed generation. There is a necessity to develop a high power density, bi-directional, EV battery charger capable of sinking or sourcing real and reactive power. However, the state of the art of EV battery chargers are unidirectional and have multiple stages of power conversion. A single phase, single stage, isolated, bi-directional SiC AC-DC converter is proposed and it is analyzed with DQ current control. Simulation and hardware results are shown confirming the analysis.

Single phase electric vehicle battery chargers require large electrolytic capacitors to filter voltage ripples in the DC bus. Bulky electrolytic capacitors are added to the DC bus to meet ripple voltage and ripple current requirements. These capacitors can be eliminated by rejecting the ripple current in the DC bus. The rip-

ple current is rejected by injecting a current of same magnitude and opposite phase into the DC bus. The current is injected in the DC bus by applying an appropriate voltage across an energy storage element through an additional half bridge. Here in this thesis, ripple rejection in a single phase bi-directional AC-DC converter is proposed and analyzed in detail. Simulation results are shown confirming the analysis.

A three phase AC-DC converter can handle more power than the single phase converter. Universal utility bi-directional AC-DC converters are useful as they can be used with either three phase power or single phase power based on the availability. Additionally, a three phase bi-directional SiC AC-DC converter is proposed and analyzed with DQ current control. Simulation results are presented verifying the analysis.

1.3 Literature review

Electric vehicle battery chargers have attracted more attention for research in the past decade. The current architecture of a typical electric vehicle battery charger is shown in Fig. 1.1. The battery charger converts the utility grid AC voltage to battery pack voltage using two stage power conversion. The first stage is an AC-DC Converter, it rectifies the AC voltage from the utility to DC voltage at unity power factor. The second stage is an isolated DC-DC converter which provides galvanic isolation with battery charging controls. The controls of the AC-DC converter and the DC-DC Converter are synchronized using a common master controller.

1.3.1 AC-DC Converter

A full bridge diode rectifier followed by a simple boost converter is commonly used as a front end AC-DC converter. A boost converter is chosen as it is

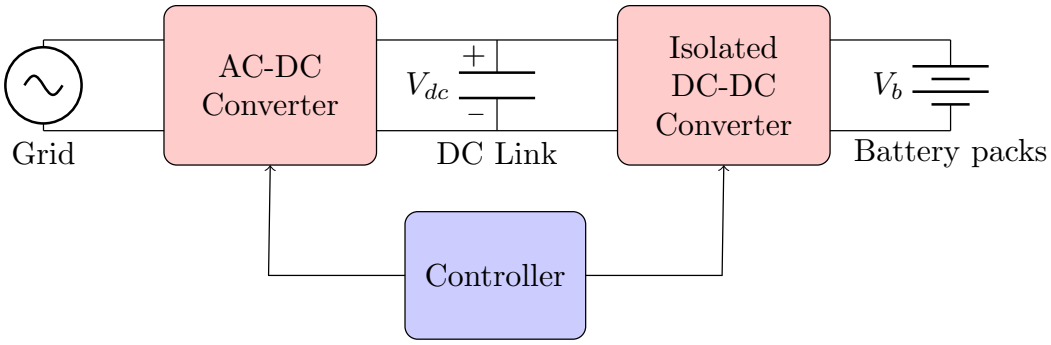

Figure 1.1: Electric vehicle battery charger architecture

simple and draws a low THD (Total Harmonic Distortion) input harmonic current from the AC grid, maintaining unity power factor. A PFC (Power factor correction) boost converter gets bulkier as the converter power increases. An interleaved PFC boost converter is preferred for high power front AC-DC converter. An interleaved PFC boost converter consists of two semiconductor devices, two boost inductors and two diodes. The required boost inductance and filter capacitance used in the interleaved PFC boost converter is lower compared to a simple PFC boost. Losses are lower in the interleaved PFC boost due to the smaller reactive elements used. The interleaved PFC boost converter has benefits such as high power density and overall high efficiency compared to single PFC boost converter.

Zero voltage switching (ZVS) is switching a semiconductor device with zero voltage across it. ZVS reduces switching losses significantly, thereby, allowing designers to operate the converter at high frequency. High frequency operation with ZVS improves efficiency and power density of the AC-DC converter. An interleaved PFC boost converter with an auxiliary circuit to implement ZVS is shown in [2].

1.3.2 Isolated DC-DC Converter

An isolated LLC (Inductor-Inductor-Capacitor) resonant DC-DC converter is used in the second stage for battery charging regulation [3]. An LLC resonant converter consists of a half bridge inverter, resonant tank, transformer and a diode bridge rectifier. LLC resonant DC-DC converters provide galvanic isolation through a transformer. They operate efficiently by implementing ZVS (Zero voltage switching) in the primary circuit and ZCS (Zero current switching) in the secondary circuit under certain operating conditions. An LLC resonant converter can operate with a wide input voltage range. This is a necessary requirement as this converter is connected to the output of the interleaved PFC boost converter which has wide output voltage variation.

1.3.3 Single phase bi-directional battery charger

The transportation industry is the second largest consumer of electricity as per the U.S. Energy Information Administration (EIA). However, 93% of the transportation energy comes from petroleum [4]. Electric utility companies are keeping up with the power demand due to the rise of electrification of transportation vehicles. The rise in the number of electric vehicles is considered as extra load, and the electric utility companies are forced to scale up the power system or increase their spinning reserves. In fact, electric vehicles can be a huge benefit to the power system as a whole. The electric energy stored in electric vehicles can be used as reserves in the power system during peak demand. Vehicle-to-grid is one such technology that allows stored energy from the batteries in electric vehicles to be sent back to the power grid for peak power requirements, voltage regulation, voltage shaving, reactive power compensation etc. Electric vehicles can also act as Distributed Generation (DG). This necessitates electric vehicle battery charging

converters to be bi-directional and capable of sinking or sourcing real and reactive power.

An active front end rectifier with high frequency dc link followed by a bi-directional isolated resonant DC-DC converter is presented in [5]. The converter topology presented above has two stage conversion enabling bi-directional power flow. Two stage power conversion reduces the system efficiency and power density as the system scales up in size. The increased number of reactive elements due to the multiple power stages reduces the system reliability. In addition, control becomes complex due to the multiple stages involved.

Earlier work on a Dual active bridge (DAB) based power converter is presented in [6]. The DAB based topology has benefits over the other converters discussed previously such as the single stage power conversion, reduced number of reactive elements, high power density and high efficiency. A universal utility interface for PHEV with V2G functionality using DAB topology is presented in [7]. This converter works with both single phase power input and three phase power input. It implements a DC bus voltage control loop and an active power control loop. This converter lacks closed loop control to sink or source real and reactive power from the grid. Current control of DAB based bi-directional AC-DC converter is presented in [8]. The input current is controlled to sink or source real and reactive power. The converter discussed above has significant harmonics in the input current due to the effect of the clamp circuit.

A high power density Silicon Carbide (SiC) based single phase bi-directional AC-DC converter with DQ current control is presented in [9]. This eliminated the harmonics in the AC input current due to the clamp circuit. Simulation and experimental results are shown in Chapter 2 confirming the analysis of a single phase bi-directional SiC AC-DC Converter.

1.3.4 DC bus Ripple current rejection in a single phase bi-directional AC-DC converter

Ripple current in the DC bus of a single phase bi-directional AC-DC converter is significant. Large electrolytic capacitors are required on the DC bus to filter out the ripple current in the DC bus. A high power density single phase active rectifier with ripple current rejection is discussed in [10]. DC Ripple Current Reduction on a Single-Phase PWM Voltage-Source Rectifier is presented in [11]. The above converters lack bi-directional power flow capability to sink or source real and reactive power and do not provide isolation.

DC ripple current rejection in an isolated, single stage, single phase bi-directional AC-DC converter with DQ current control is presented in Chapter 3. The ripple current in the DC bus is rejected by injecting a current 180° out of phase with the ripple current. The desired current is injected by applying an appropriate voltage across an energy storage element using an additional half-bridge inverter. Average inverter leg currents are derived over a switching cycle T_s and are found to have distinct unbalanced current profile. Simulation results will show the rejection of the ripple current in the DC bus under various operating conditions.

1.3.5 Three phase bi-directional AC-DC converter

A novel three phase bi-directional AC-DC converter is presented in [7]. It implements a complex closed loop control system to control DC bus voltage and active power flow. It discusses a phase shift modulation strategy which induces harmonics in the AC input current. A new modulation strategy is proposed in [12] which overcomes the problems in [7] but lacks closed loop control to sink or source real and reactive power.

A three phase bi-directional SiC AC-DC converter with DQ current control is presented in Chapter 4. Analysis of the three phase bi-directional SiC AC-DC converter is performed. Simulation results are shown verifying the converter's ability to sink or source real and reactive power under various operating conditions.

CHAPTER 2

SINGLE PHASE BI-DIRECTIONAL SIC AC-DC CONVERTER

2.1 Introduction

Electric vehicles (EV) play a major part in reducing the carbon footprint due to fuel consumption in the transportation sector [13]. The stored energy in the electric vehicle batteries are unused while parked. This stored energy can be returned back to the grid during peak demand which is known as Vehicle-to-grid (V2G) energy transfer [14]. Electric vehicles with V2G functionality offer other benefits like voltage regulation, voltage shaving, reactive power compensation and distributed generation. This necessitates electric vehicle battery charging converters to be bi-directional and capable of sinking or sourcing real and reactive power.

Various bi-directional AC-DC converters based on Dual Active Bridge (DAB) have been presented in [7,15–21]. The above converters lack closed loop control to sink or source the real and reactive power. DQ current control of a bi-directional AC-DC converter is presented in [22] and its experimental results are shown in [8]. The results shown in [8] have harmonic distortion in the input current $i_i(t)$ due to a clamp circuit. This chapter focuses on the design and implementation of a high power density, isolated, single-stage, bi-directional SiC AC-DC converter with the elimination of the clamp circuit effects on the input current $i_i(t)$.

High power density is achieved by using Silicon Carbide (SiC) devices instead of the conventional silicon devices [23–26]. Operating SiC devices at high frequency (100 kHz) significantly reduces the size of the filter components and generates lower switching losses compared to silicon devices. They operate at high temperature allowing designers to choose a smaller heat sink, thus saving in cost of the overall system design.

In this chapter, analysis of a single phase bi-directional AC-DC converter is discussed. Simulation results are presented for various operating conditions. Experimental results are shown to verify the simulation results.

2.2 Analysis

Analysis of a Dual Active Bridge (DAB) based bi-directional AC-DC converter is presented in this section. The topology shown in Fig. (2.1) consists of a single phase matrix converter ($S_{1,P}$, $S_{1,N}$, $S_{2,P}$, $S_{2,N}$, $S_{3,P}$, $S_{3,N}$, $S_{4,P}$, $S_{4,N}$), a single phase inverter (S_5, S_6, S_7, S_8), a LC filter and a high frequency transformer. Assuming the voltage drop across the filter inductor L_f is zero, the input voltage $v_i(t)$ with angular frequency $\omega_i(t)$ as shown in (2.1) is applied across the single phase matrix converter.

$$v_i(t) = \hat{V}_i \cos(\omega_i t) \tag{2.1}$$

The input current $i_i(t)$ can be controlled through the matrix converter current $i_m(t)$ [27]. The duty cycle $d(t)$ of the converter is shown in (2.2) and it is related to the average matrix converter current $i_m(t)$ in (2.3). The average matrix converter current $i_m(t)$ shown in (2.6) is obtained by substituting (2.4) & (2.5) in (2.3). The magnitude and the phase angle of the average matrix converter current $i_m(t)$ (2.6) can be controlled by controlling δ and ϕ respectively.

$$d(t) = \frac{|v_i(t)|\, n}{V_d} \tag{2.2}$$

$$\bar{i}_m(t) = \frac{n\delta V_d}{4Lf_s} d(t) \tag{2.3}$$

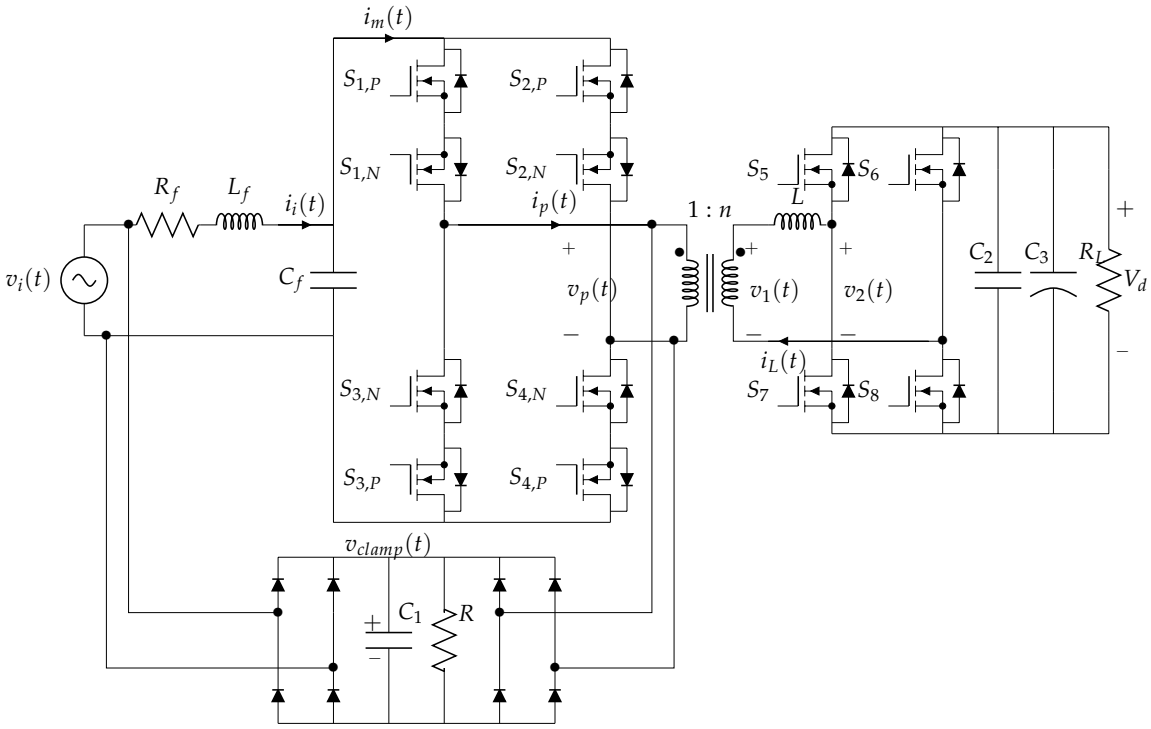

Figure 2.1: Topology of a single phase bi-directional AC-DC Converter

$$d(t) = \frac{\left|\hat{V}_i \cos(w_i t + \phi_m)\right| n}{V_d} \tag{2.4}$$

$$K_b = \frac{n^2 \hat{V}_i}{4 L f_s} \tag{2.5}$$

$$\bar{i}_m(t) = K_b \delta \cos(w_i t + \phi_m) \tag{2.6}$$

From the LC filer dynamics, the input current $i_i(t)$ can be related to the matrix converter current $i_m(t)$ in (2.7). As seen from (2.7), it is difficult to control the input current $i_i(t)$ due to sinusoids being involved. The two stationery reference frame variables are obtained by delaying the actual input current $i_i(t)$ by $\frac{\pi}{2}$ rad.

The stationery reference frame variables (i_α, i_β) are transformed into rotating reference frame variables (i_d, i_q). The rotating reference frame variables (i_d, i_q) are dc quantities which can be controlled using simple PI controllers.

$$i_m(t) = L_f C_f \frac{\mathrm{d}^2}{\mathrm{dt}^2} i_i(t) + R_f C_f \frac{\mathrm{d}}{\mathrm{dt}} i_i(t) + i_i(t) - C_f \frac{\mathrm{d}}{\mathrm{dt}} v_i(t) \tag{2.7}$$

By substituting (2.8) into (2.7) and equating the real and imaginary components gives $i_{md}(t)$ & i_{mq} as shown in (2.9) & (2.10).

$$X(t) = X_d(t)\cos(wt) - X_q(t)\sin(wt) \tag{2.8}$$

$$\begin{aligned} i_{md}(t) = {} & L_f C_f \left[\frac{\mathrm{d}^2}{\mathrm{dt}^2} i_{id}(t) - 2\omega_i \frac{\mathrm{d}}{\mathrm{dt}} i_{iq}(t) - \omega_i^2 i_{id}(t) \right] \\ & + R_f C_f \left[\frac{\mathrm{d}}{\mathrm{dt}} i_{id}(t) - \omega_i i_{iq}(t) \right] + i_{id}(t) - C_f \frac{\mathrm{d}}{\mathrm{dt}} v_{id}(t) \end{aligned} \tag{2.9}$$

$$\begin{aligned} i_{mq}(t) = {} & L_f C_f \left[\frac{\mathrm{d}^2}{\mathrm{dt}^2} i_{iq}(t) + 2\omega_i \frac{\mathrm{d}}{\mathrm{dt}} i_{id}(t) - \omega_i^2 i_{iq}(t) \right] \\ & + R_f C_f \left[\frac{\mathrm{d}}{\mathrm{dt}} i_{iq}(t) + \omega_i i_{id}(t) \right] + i_{iq}(t) - C_f \omega_i v_{id}(t) \end{aligned} \tag{2.10}$$

Decoupling terms (2.11), (2.12) are added to (2.9) and (2.10) to independently control $i_{id}(t)$ and $i_{iq}(t)$ [28].

$$i_{dcd}(t) = -2\omega_i L_f C_f \frac{d}{dt} i_{iq}(t) - \omega_i R_f C_f i_{iq}(t) \tag{2.11}$$

$$i_{dcq}(t) = 2\omega_i L_f C_f \frac{d}{dt} i_{id}(t) + \omega_i R_f C_f i_{id}(t) \tag{2.12}$$

Proportional Integral (PI) controllers are implemented to drive the steady state error to zero between the reference input currents $i^*_{id}(t)$ & $i^*_{iq}(t)$ and the actual input currents $i_{id}(t)$ & $i_{iq}(t)$. The PI controller's response $i^*_{pid}(t)$ and $i^*_{piq}(t)$ are shown in (2.13) and (2.14).

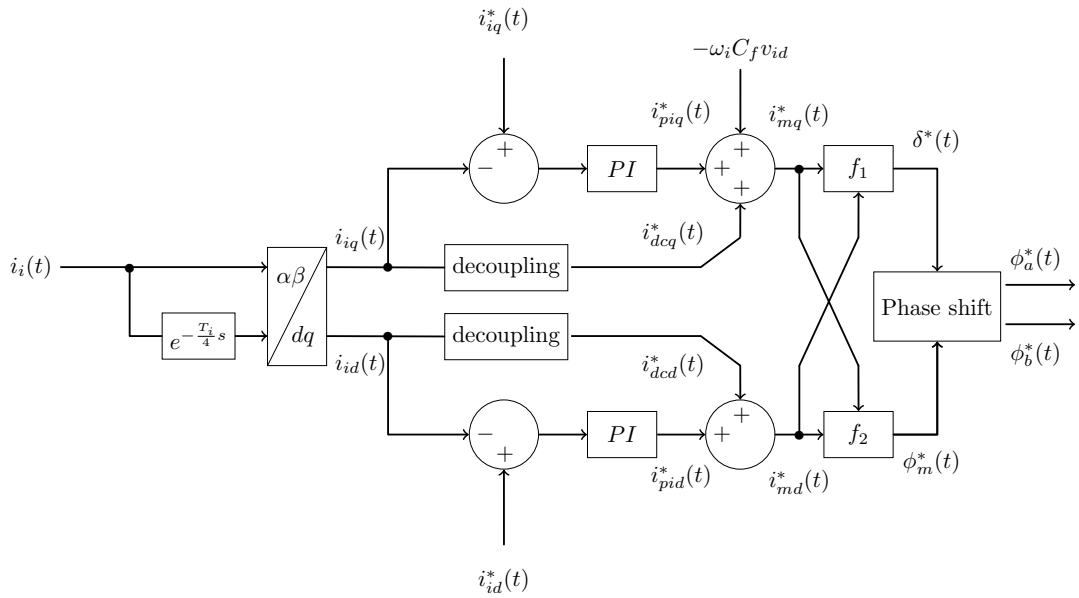

Figure 2.2: Control diagram of a single phase bi-directional AC-DC converter

$$i_{pid}{}^*(t) = K_p \left(i_{id}{}^*(t) - i_{id}(t) \right) + K_i \int \left(i_{id}{}^*(t) - i_{id}(t) \right) dt \tag{2.13}$$

$$i_{piq}{}^*(t) = K_p \left(i_{iq}{}^*(t) - i_{iq}(t) \right) + K_i \int \left(i_{iq}{}^*(t) - i_{iq}(t) \right) dt \tag{2.14}$$

A closed loop transfer function $G_{cl}(s)$ (2.15) is obtained from the converter equations and the control diagram as shown in Fig. 4.2. A suitable gain and bandwidth is chosen in order to obtain a stable closed loop system and a good transient response. Lastly, the values of K_p and K_i are determined.

$$G_{cl}(s) = \frac{\left(K_p s + K_i \right)}{L_f C_f s^3 + C_f R_f s^2 + (1 - \omega_i^2 L_f C_f + K_p) s + K_i} \tag{2.15}$$

From the reference currents $i_{md}^*(t)$ and $i_{mq}^*(t)$, the control variables $\delta^*(t)$ and $\phi^*(t)$ can be calculated from (2.16) and (2.17).

Table 2.1: Simulation setup of a single phase bi-directional AC-DC converter

Filter inductance, L_f	$43.7\mu H$
Filter capacitance, C_f	$12\mu F$
Internal resistance of filter inductor, R_f	0.1Ω
Leakage inductance of the High frequency transformer, L	$7\mu H$
Clamp capacitance, $C1$	$6\mu F$
DC link capacitance 1, $C2$	$110\mu H$
DC link capacitance 2, $C3$	$2000\mu F$
Input AC peak, $\hat{V}_i$	$240\sqrt{2}V$
Input AC frequency, ω_i	$2\pi 60\ \frac{rad}{s}$
Switching frequency, f_s	$100kHz$
Propositional gain, K_p	0.01
Integral gain, K_i	65
Load resistance, R_L	100Ω

$$\delta^*(t) = \text{sgn}({i_{md}}^*(t))\frac{1}{K_b}\sqrt{{i_{md}}^*(t)^2 + {i_{mq}}^*(t)^2} \tag{2.16}$$

$$\phi_m^*(t) = \tan^{-1}\left(\frac{{i_{mq}}^*(t)}{{i_{md}}^*(t)}\right) \tag{2.17}$$

The duty cycle of the half bridges (S_5, S_7) and (S_6, S_8) are fixed at 50%. The phase shift of the half bridges (S_5, S_7) and (S_6, S_8) are $\phi_a^*(t)$ and $\phi_b^*(t)$ calculated from (2.18) and (2.19) respectively.

$$\phi_a^*(t) = \frac{\pi}{2}\left[\frac{n\hat{V}_m}{V_d}\cos(w_i t + \phi_m^*(t)) + \delta^*(t)\right] \tag{2.18}$$

$$\phi_b^*(t) = \frac{\pi}{2}\left[-\frac{n\hat{V}_m}{V_d}\cos(w_i t + \phi_m^*(t)) + \delta^*(t)\right] \tag{2.19}$$

2.3 Simulation

The topology shown in Fig. 2.1 is modeled in PLECS using the parameters shown in Table 2.1. The half bridges are modulated using phase shifts $\phi_a^*(t)$ and

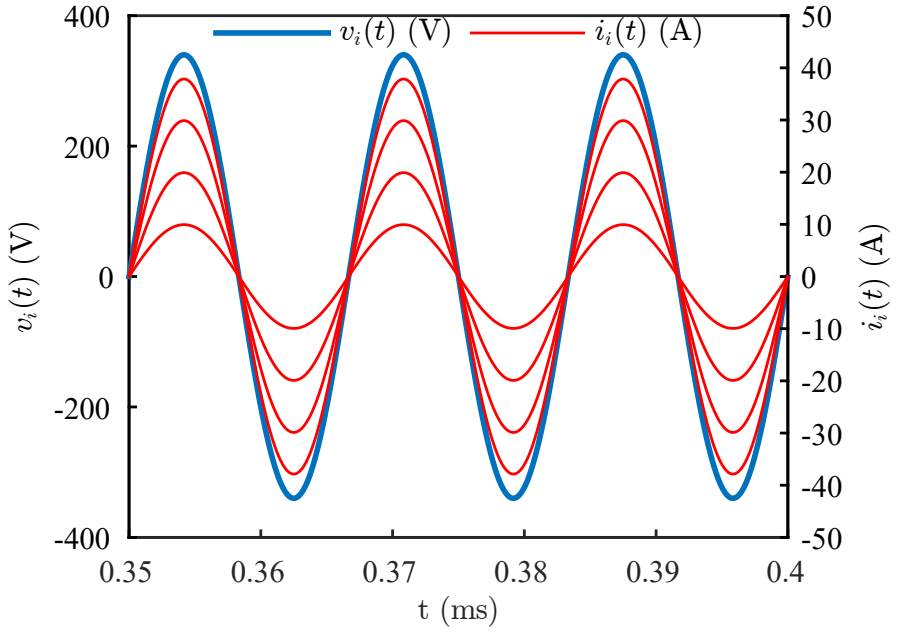

Figure 2.3: Simulation results: (i_{id}, i_{iq}) = (10, 0), (20, 0), (30, 0), (38.885, 0) A

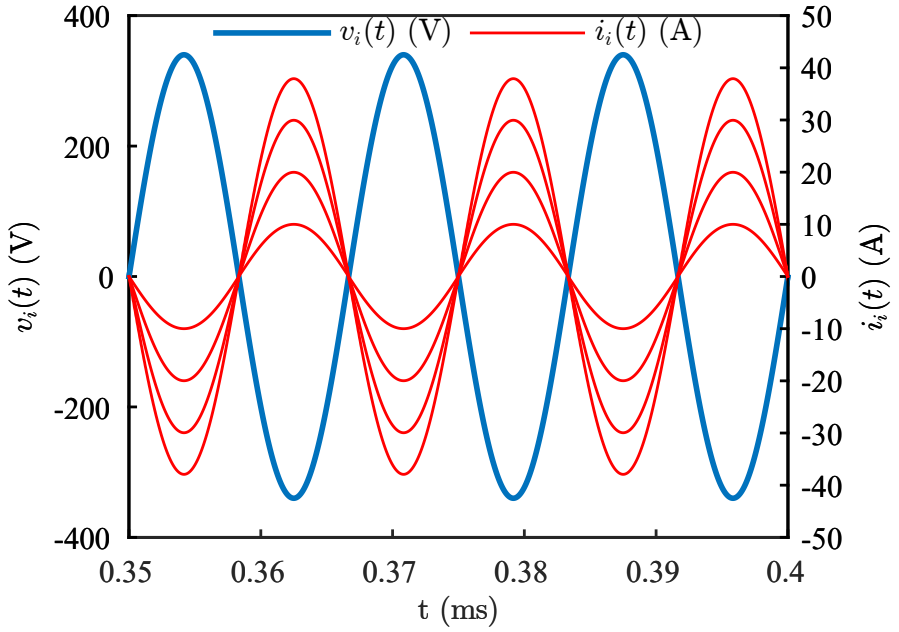

Figure 2.4: Simulation results: (i_{id}, i_{iq}) = (-10, 0), (-20, 0), (-30, 0), (-38.885, 0) A

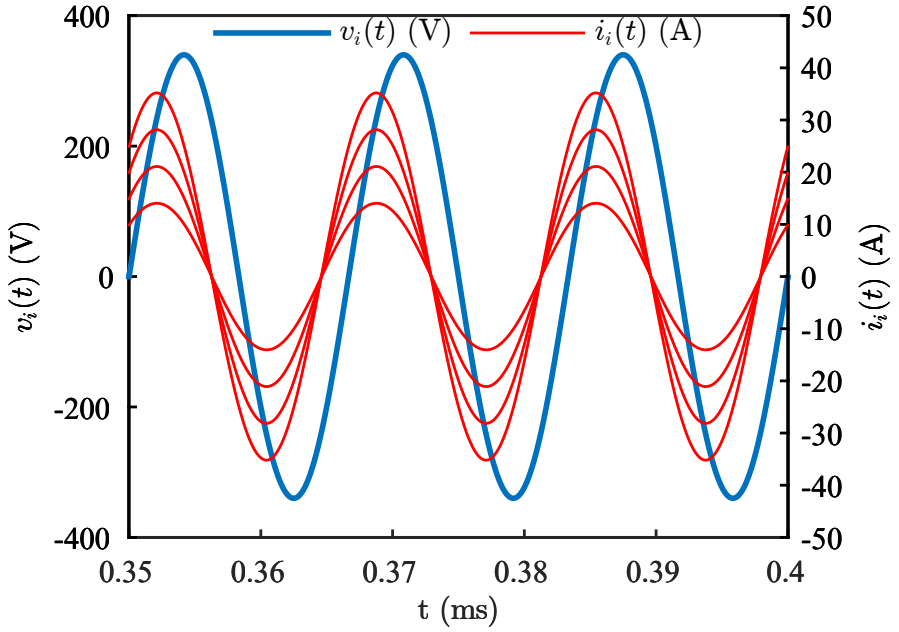

Figure 2.5: Simulation results: (i_{id}, i_{iq}) = (10, 10), (15, 15), (20, 20), (25, 25) A

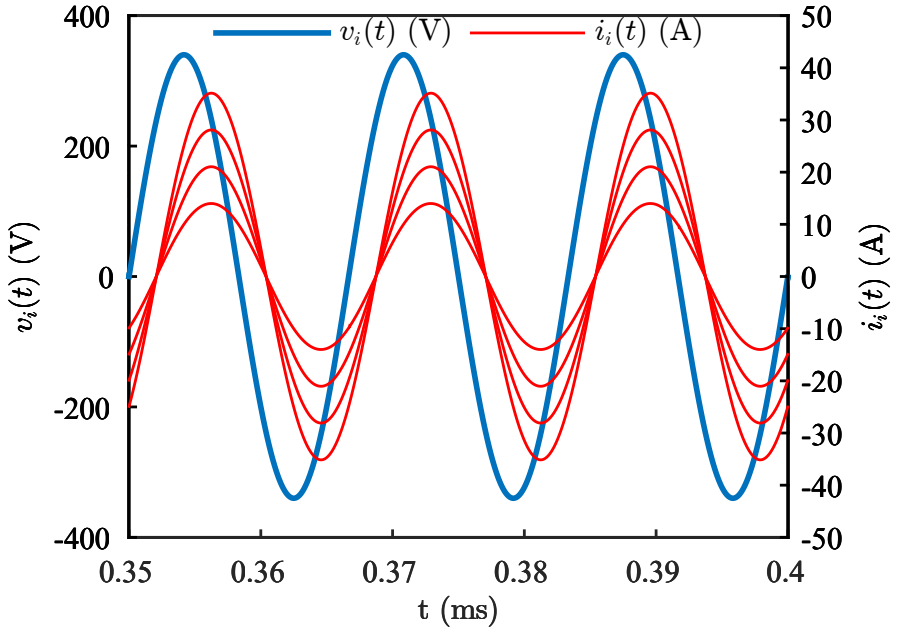

Figure 2.6: Simulation results: (i_{id}, i_{iq}) = (10, -10), (15, -15), (20, -20), (25, -25) A

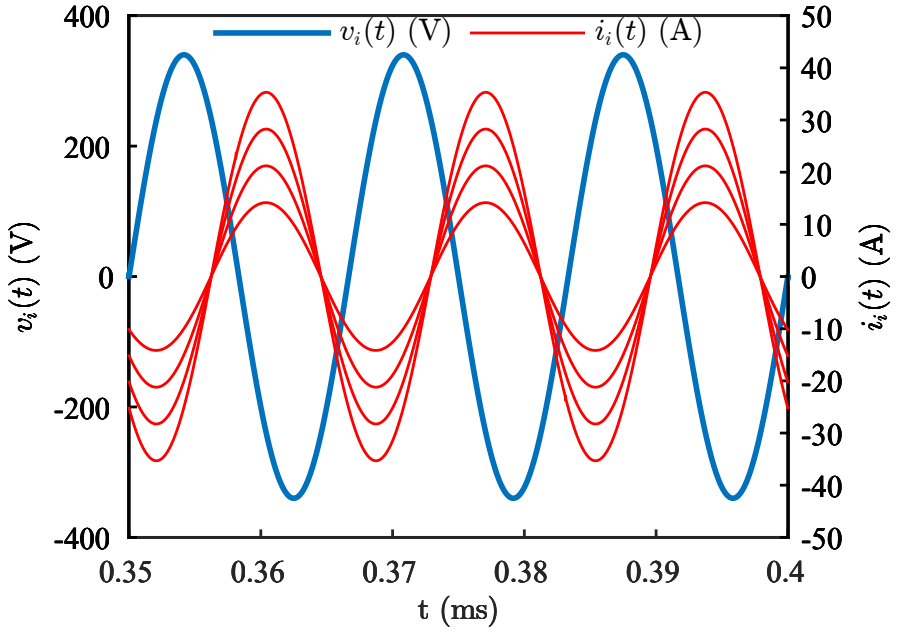

Figure 2.7: Simulation results: (i_{id}, i_{iq}) = (-10, -10), (-15, -15), (-20, -20), (-25, -25) A

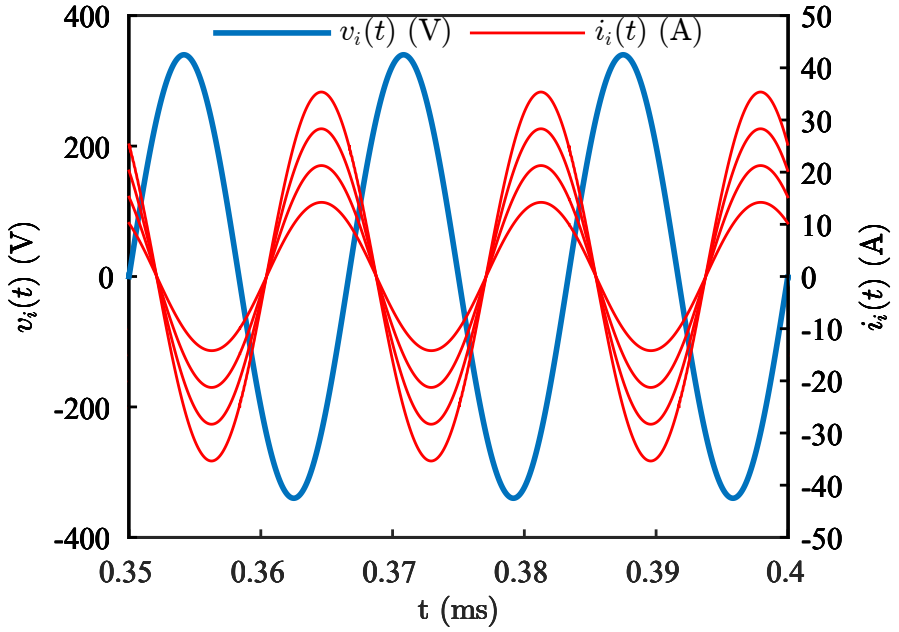

Figure 2.8: Simulation results: (i_{id}, i_{iq}) = (-10, 10), (-15, 15), (-20, 20), (-25, 25) A

Table 2.2: Control variables of a single phase bi-directional AC-DC converter

i_{id}^*	i_{iq}^*	δ^*	ϕ^*
+	+	+	+
+	−	+	−
−	−	−	−
−	+	−	+

$\phi_a^*(t)$ based on $i_{id}^*(t)$ and $i_{iq}^*(t)$ input commands as shown in the control diagram Fig. 4.2. All the switches and diodes used in the simulation model are ideal.

Table 2.2 shows the signs of the control variables for various input current commands. Simulation results in Fig. 4.3 - 4.8 show the input voltage $v_i(t)$ and various levels of input current $i_i(t)$ depicting real and reactive power sourcing or sinking into the AC grid. Fig. 2.3 shows pure real power sourcing from the AC grid, here the battery charger acts like a resistive load. Fig. 2.4 shows pure real power sinking into the AC grid, here the battery charger acts like an ideal generator. Fig. 2.5 shows real and reactive power sourcing from the AC grid, here the battery charger acts like an inductive load. Fig. 2.6 shows real power sourcing from the AC grid and reactive power sinking into the AC grid, here the battery charger acts like a capacitive load. Fig. 2.7 shows real and reactive power sinking into the AC grid, here the battery charger acts like an over excited synchronous generator. Fig. 2.8 shows real power sinking into the AC grid and reactive power sourcing from the AC grid, here the battery charger acts like an under excited synchronous generator. The simulation results show the converter's ability to sink or source real and reactive power into the AC grid.

2.4 Hardware

2.4.1 Single phase matrix converter and Inverter

The single phase matrix converter consists of four bi-directional switches. Each bi-directional switch consists of a two source-tied SiC MOSFET's. The single phase matrix converter is composed of switches ($S_{1,P}$, $S_{1,N}$), ($S_{2,P}$, $S_{2,N}$), ($S_{3,P}$, $S_{3,N}$), ($S_{4,P}$, $S_{4,N}$). Bi-directional switches are capable of four quadrant operation i.e., they block positive and negative voltages and allow current in positive and negative directions. The single phase inverter is composed of SiC MOSFET switches S_5, S_6, S_7, S_8. Dedicated SiC MOSFET gate drivers are used for driving these switches which additional-ly provides optical isolation. Gate driver voltage levels used are $V_{gs,on}$ +15 V and $V_{gs,off}$ -5 V.

2.4.2 Clamp circuit

The clamp circuit shown in Fig. 2.1 consists of a bridge rectifier connected to the primary of the high frequency transformer. SiC schottky diodes are used in the bridge rectifier. SiC schottky diodes are suitable for high frequency rectification because they have essentially zero reverse recovery losses. A line frequency diode bridge rectifier charges the polypropylene capacitor to the peak of the input voltage $\bar{V}_i$. The clamp circuit applies the capacitor voltage across the primary of the high frequency transformer during false current commutation. This protects the matrix converter switches from high voltage spikes. A suitable resistor is connected in parallel to the capacitor for voltage balancing.

Table 2.3: Hardware components of a single phase bi-directional AC-DC converter

Components	**Description**
SiC Mosfet switches	CMF20120D, 1200V, 43A
SiC Schottky diodes	C4D30120D, 1200V, 30A
SiC Gate drive optocoupler	ACPL-W346, 2.5 A
Gate drive power supply	RP-1212D, 1A, RP-1205S, 1A, LM2595, 1A
Clamp capacitor, C_1	6 μF, Polypropylene capacitor, 450V
DC capacitor, C_2	110 μF, Polypropylene capacitor, 450V, Low ESR
DC capacitor, C_3	2 $\times$ 1000 μF, Aluminum capacitor, 500V, 5.43A RMS
AC filter capacitor, C_f	2 $\times$ 6 μF, Polypropylene capacitor
AC filter inductor, L_f	43.7μH ferrite core, μ_r 60, Magnetics Kool Mμ, 00K5530E060
High frequency transformer	1:1 turns ratio, ferrite core, 11 turns, 7 μH leakage inductance L, 0R49928EC
Voltage sensor	LV-25P
Current sensor	LTS-25 NP
Digital signal controller	dsPIC33EP512MU810

2.4.3 Capacitor and Magnetic selection

A polypropylene capacitor C_2 is connected to the DC bus and placed close to the inverter switches to provide a low impedance path for the high frequency switching current. Two $1000\mu F$ electrolytic capacitors $C2$ are used to meet the ripple voltage $\hat{V}_{d2}$ (3% of $\hat{V}_d$) and ripple current $\hat{I}_{d2}$ (13 A RMS) requirement in the DC bus as shown in (2.20), (2.21) from [29].

$$\hat{I}_{d2} = \frac{1}{2}\frac{\hat{V}_s}{\hat{V}_d} I_L \tag{2.20}$$

$$\hat{V}_{d2} = \frac{\hat{I}_L}{4\omega C_1}\frac{\hat{V}_s}{\hat{V}_d} \tag{2.21}$$

A LC filter is used to filter input current harmonics from the matrix converter switching [30–32]. Two $6\mu F$ polypropylene capacitors C_f and a $43.7\mu H$ ferrite core inductor are used in the filter. A 1:1 turns ratio ferrite core based high frequency transformer with 7 μH leakage inductance L is used.

2.4.4 Sensors

Voltages and currents in the converter are sensed using a voltage transducer (LV-25P) and a current transducer (LTS-25 NP) respectively. The input voltage $v_i(t)$, input current $i_i(t)$ and the clamp voltage $V_{clamp}(t)$ are sensed and filtered using a 2^{nd} order unity gain sallen key filter with a 10 kHz cut off frequency. The transformer primary current $i_p(t)$ is filtered using a 1^{st} order RC differential amplifier at a 1 MHz cut off frequency.

2.5 Firmware

Modulation of the single phase matrix converter and the inverter are implemented in a Microchip dsPIC33EP512MU810. The control loop is updated every 20μs (50 kHz). All the hardware filtered signals are simultaneously sampled and converted using built-in 10 bit ADC peripheral and sampling is triggered by inverter PWM module for synchronization. The ADC signals are filtered using a 16 pt. moving average to reduce switching noise. The filtered signals are checked for over-voltage and over-current faults. Protection is implemented by opening a relay connected to the AC mains and disabling all the switches.

Table 2.4: Computation time of a single phase bi-directional AC-DC converter

Modules	**time (μs)**
Moving average filter	3.2
Protection	1.0
PLL (θ)	1.5
Sin(θ),Cos(θ)	0.7
Parks transformation ($\alpha\beta \rightarrow dq$)	0.5
PI controller	2 x 0.5
Angle (atan2)	1.2
Magnitude ($\sqrt{x^2 + y^2}$)	1
Duty cycle calculation	1.5
Total	**11.6**

The input current $i_i(t)$ is delayed by $\frac{\pi}{2}$ rads to generate the stationary reference frame variables $i_{i,\alpha\beta}$. A phase frequency detector (PFD) based PLL is implemented to lock on to the phase angle of the input voltage $v_i(t)$. The stationary reference frame variables $v_{i,\alpha\beta}$, $i_{i,\alpha\beta}$ are transformed to rotating reference frame variables $v_{i,dq}$, $i_{i,dq}$ using a DQ transformation. The control variables $i_{id}(t)$ and $i_{iq}(t)$ are now dc values which can be easily controlled using a Proportional Integral (PI) controller. The controller drives the steady state error between $i_{id}(t)$ & $i^*_{id}(t)$ and $i_{iq}(t)$ & $i^*_{iq}(t)$ to zero.

The magnitude and angle of the matrix converter currents are computed using approximations [33, 34]. From equation (4.12) and (2.17), the control variables $\delta^*(t)$ and $\phi^*(t)$ can be computed. The inverter is modulated at 100 kHz switch-

ing frequency with duty-cycle $d(t)$ calculated from (3.19). The matrix converter is modulated with a 50% fixed duty-cycle with four step current commutation. The direction of transformer primary current $i_p(t)$ is detected in real time using the in-built comparator for current commutation. An incorrect current direction will engage the clamp circuit which introduces harmonic distortion in the input current $i_i(t)$. Error in detecting current direction close to zero is significantly reduced by using analog comparators. This mitigates the effect of clamp circuit acting during false current commutation. Computation time taken for each module is tabulated in Table 2.4

Table 2.5: Hardware setup of a single phase bi-directional AC-DC converter

Filter inductance, L_f	$43.7\mu H$
Filter capacitance, C_f	$12\mu F$
Leakage inductance of the High frequency transformer, L	$7\mu H$
Clamp capacitance, $C1$	$6\mu F$
DC link capacitance 1, $C2$	$110\mu H$
DC link capacitance 2, $C3$	$2000\mu F$
Input AC peak, $\hat{V}_i$	$110\sqrt{2}$ V
Input AC frequency, ω_i	$2\pi 60 \frac{rad}{s}$
Switching frequency, f_s	$100\ kHz$
Propositional gain, K_p	0.0039
Integral gain, K_i	0.0039
Load resistance, R_L	90Ω

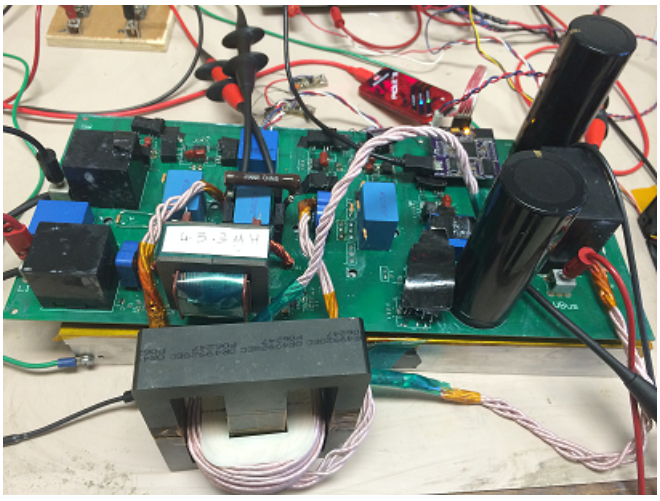

Figure 2.9: Hardware setup of a single phase bi-directional AC-DC converter

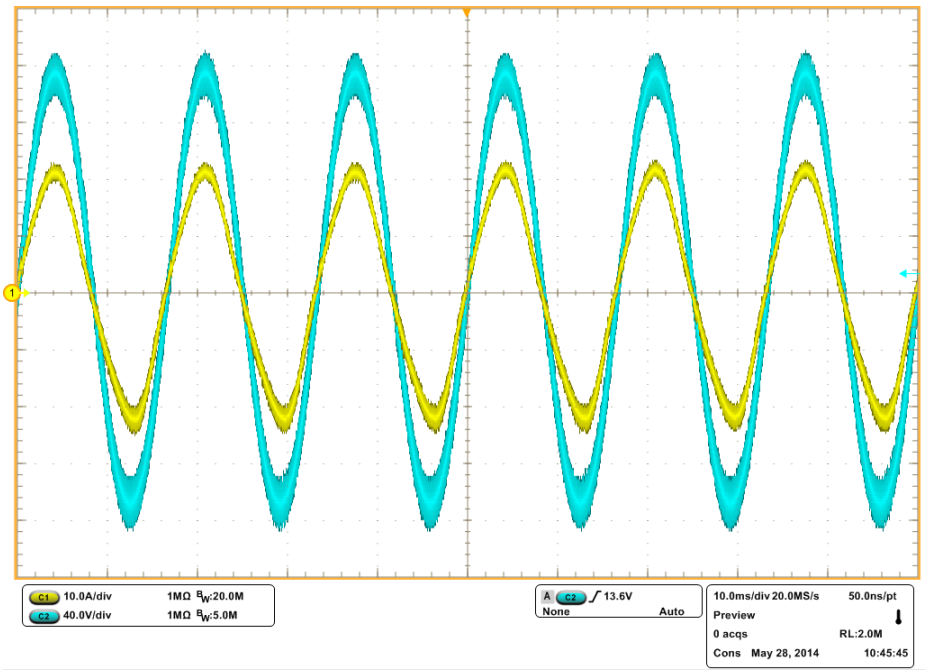

Figure 2.10: Hardware results: Input current $i_i(t)$(yellow), Input voltage $v_i(t)$(blue)

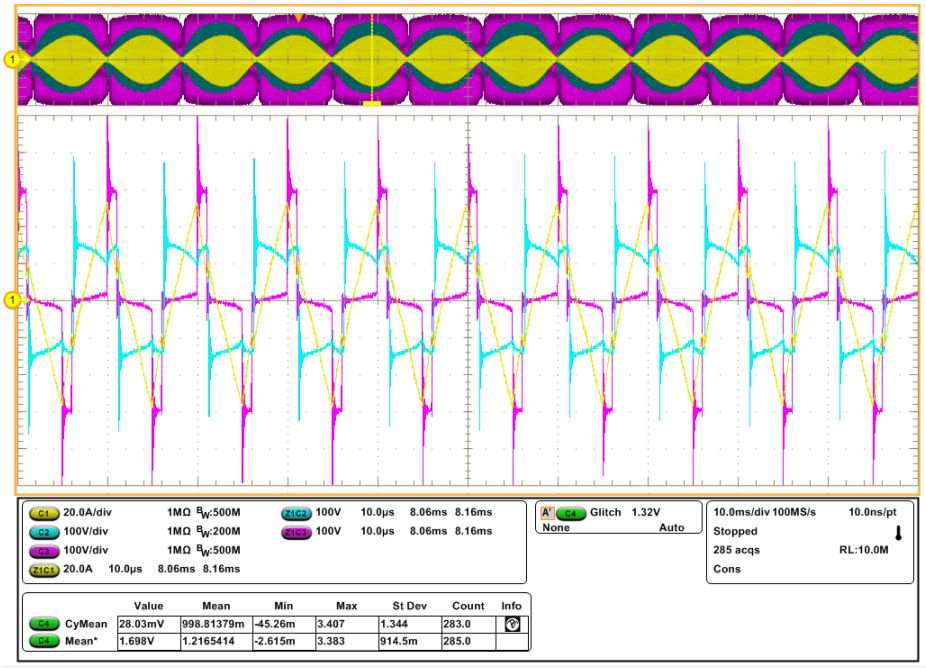

Figure 2.11: Hardware results: Transformer primary current and voltage $i_p(t)$(yellow),$v_p(t)$(blue), Inverter voltage $v_2(t)$ (magenta)

2.6 Hardware Results

Hardware results are recorded based on the conditions in Table 2.5. Fig. 2.10 shows the input voltage $v_i(t)$ (blue) and the input current $i_i(t)$ (yellow) with a reference current of $i_{id}(t) = 22\text{A}$ and $i_{iq}(t) = 0\text{A}$. The DC bus voltage V_d is maintained at 300 V to transfer 1 kW active power into a 90 Ω resistive load. It is seen from the input current $i_i(t)$ that the harmonic distortion due the effect of clamp circuit is mitigated. Experimental hardware setup is shown in Fig. 2.9. Fig. 2.11 shows the transformer primary current $i_p(t)$ (yellow), transformer primary voltage $v_p(t)$ (blue) and the inverter voltage $v_2(t)$ (magenta).

CHAPTER 3

DC RIPPLE CURRENT REJECTION IN A SINGLE PHASE BI-DIRECTIONAL SIC AC-DC CONVERTER

3.1 Introduction

Single phase bi-directional AC-DC converters shown in [7–9, 15–22, 35–37] require large electrolytic capacitors to meet the ripple current and ripple voltage requirements of the DC bus. Aluminum electrolytic capacitors are bulky, costly, and also suffer from reliability issues [38–42]. Electrolytic capacitors can be eliminated by rejecting the ripple current in the dc bus.

A dual active bridge (DAB) based bi-directional, single phase, isolated, single stage SiC AC-DC converter with ripple current rejection in the dc bus is discussed in this chapter. A current of same magnitude and 180° out of phase with the dc ripple current is injected into the dc bus to reject (eliminate) the ripple current in the dc bus. The out of phase current is injected into the dc bus through an energy storage element by applying an appropriate voltage across it. The desired voltage is applied through an additional half-bridge.

In this chapter, analysis of the converter is performed including the ripple rejection technique using the additional half-bridge. A mathematical expression of the voltage magnitude and phase angle to be applied across the energy storage element is derived for various operating conditions. Average inverter leg currents are derived over a switching cycle to showcase the distinct current profile. Simulation results are shown with various operating conditions to verify the analysis of the converter with ripple rejection.

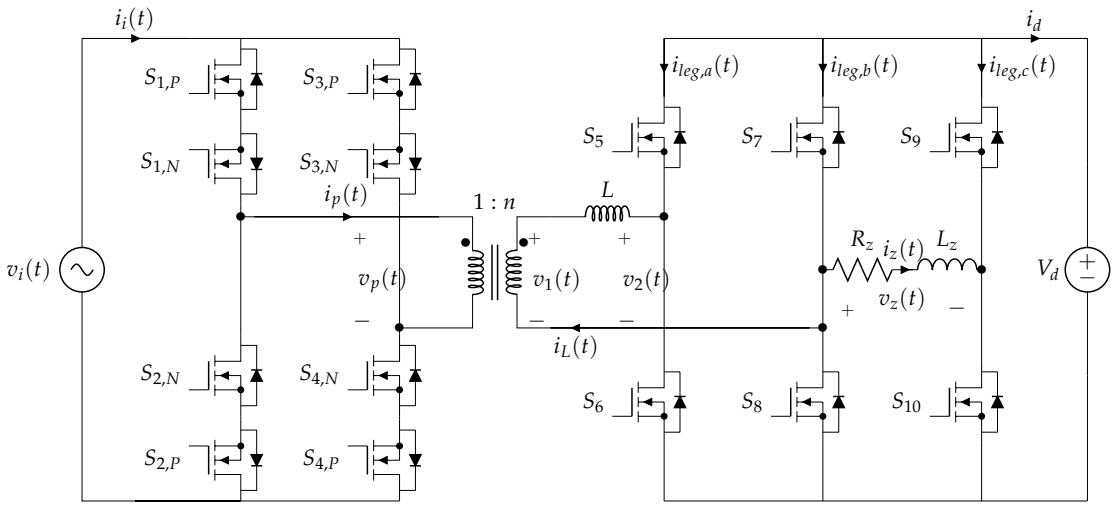

Figure 3.1: Topology of a single phase AC-DC Converter with ripple rejection

3.2 Analysis

Analysis of a Dual Active Bridge (DAB) based AC-DC converter with ripple current rejection in the DC bus is presented in this section. The converter shown in Fig. 3.1 consists of a single phase matrix converter $S_{1,P}$, $S_{1,N}$, $S_{2,P}$, $S_{2,N}$, $S_{3,P}$, $S_{3,N}$, $S_{4,P}$, $S_{4,N}$, a full bridge inverter Leg a (S_5, S_6), Leg b (S_7, S_8) and an half-bridge inverter Leg c (S_9, S_{10}). The single phase matrix converter consists of four bi-directional switches ($S_{1,P}$, $S_{1,N}$), ($S_{2,P}$, $S_{2,N}$), ($S_{3,P}$, $S_{3,N}$), ($S_{4,P}$, $S_{4,N}$) allowing bi-directional power flow between the AC grid and the DC bus. The full bridge inverter Leg a (S_5, S_6) and Leg b (S_7, S_8) are phase shift modulated for bi-directional power flow and the half-bridge inverter Leg c (S_9, S_{10}) is utilized for rejecting the ripple current in the dc bus. The input voltage v_i (3.1) with angular frequency ω_i is applied to the input of the matrix converter.

$$v_i(t) = \hat{V}_i \sin(w_i t) \tag{3.1}$$

The duty cycle d of the full bridge inverter is shown in (3.2) with a controllable phase angle ϕ_i [22]. The average input current $i_i(t)$ is shown in (3.4) with

control variables δ and ϕ_i to control the magnitude and phase angle of the average input current respectively.

$$d(t) = \frac{\left|\hat{V}_i \sin(w_i t + \phi_i)\right| n}{V_d} \tag{3.2}$$

$$K_b = \frac{n^2 \hat{V}_i}{4 L f_s} \tag{3.3}$$

$$\bar{i}_i(t) = K_b \delta \sin(w_i t + \phi_i) \tag{3.4}$$

The average dc bus current $\bar{i}_d$ is obtained by equating the input power to the output power (3.5) assuming a lossless system. From (3.1), (3.4) & (3.5), the average dc bus current $\bar{i}_d$ is obtained in (3.6). The average dc bus current contains a dc component and a ac ripple component at twice the line frequency (120 Hz). Large electrolytic capacitors are used to filter the low frequency (120 Hz) ripple current. These bulky electrolytic capacitors can be eliminated by rejecting the ripple current in the DC bus. The ripple current can be rejected by injecting a current 180° in reference to the ripple current $\bar{i}_{d,ac}(t)$.

$$\bar{i}_d(t) = \frac{v_i(t)\bar{i}_i(t)}{V_d} \tag{3.5}$$

$$\begin{aligned} \bar{i}_d(t) &= i_{d,dc} + \bar{i}_{d,ac}(t) \\ &= \frac{n^2 \hat{V}_i^2}{8 L f_s V_d} \delta \left[\cos(\phi_i) - \cos(2\omega_i t + \phi_i)\right] \end{aligned} \tag{3.6}$$

By applying an appropriate voltage across an energy storage element Z, a current 180° in reference to the ripple current $\bar{i}_{d,ac}(t)$ can be injected into the DC bus. The required voltage can be generated using an half-bridge inverter leg c

(S_9, S_{10}). The energy storage element is depicted as an inductor. Note this inductor can be an external inductor or one can utilize the EV's motor windings. The average voltage $\bar{v}_z$ across the energy storage element with a phase angle ϕ_v is shown in (3.8). The average current flowing through the energy storage element, $\bar{i}_z$, is shown in (3.9).

$$\begin{aligned} Z &= R_z + j\omega_i L_z \\ \hat{Z} &= \sqrt{R_z^2 + (\omega_i L_z)^2} \\ \phi_z &= \tan^{-1}\left(\frac{\omega_i L_z}{R_z}\right) \end{aligned} \tag{3.7}$$

$$\bar{v}_z(t) = \hat{V}_z \sin(\omega_i t + \phi_v) \tag{3.8}$$

$$\bar{i}_z(t) = \frac{\hat{V}_z}{\hat{Z}} \sin(\omega_i t + \phi_v - \phi_z) \tag{3.9}$$

The inverter leg a and leg b are operated with a fixed duty cycle at 50% (3.10) and phase shift modulated [22]. The inverter leg c is operated with a duty cycle d_c (3.11) to modulate the magnitude and phase angle of the voltage $\bar{v}_z$ applied across the energy storage element. The average ripple rejection current $\bar{i}_{rej}$ is the sum of leg c current $\bar{i}_{leg,c}$ and part of the leg b current $\bar{i}_{leg,b}$ drawn due to Z. The average ripple rejection current $\bar{i}_{rej}$ is calculated from (3.12) by substituting (3.9)-(3.11) in (3.12) to obtain (3.13).

$$d_a = d_b = \frac{1}{2} \tag{3.10}$$

$$d_c(t) = \frac{1}{2} - \frac{\hat{V}_z}{V_d} \sin(\omega_i t + \phi_v) \tag{3.11}$$

$$\bar{i}_{rej}(t) = \bar{i}_z(t)\,(d_b - d_c(t)) \tag{3.12}$$

$$\begin{aligned}\bar{i}_{rej}(t) &= i_{rej,dc} + \bar{i}_{rej,ac}(t) \\ &= \frac{\hat{V}_z^2}{2\hat{Z}V_d}\left[\cos(\phi_z) - \cos(2\omega_i t + 2\phi_v - \phi_z)\right]\end{aligned} \tag{3.13}$$

By comparing the magnitude and phase angle of the ac component in (3.6) & (3.13), the required magnitude $\hat{V}_z$ and the phase angle ϕ_v of the voltage $\bar{v}_z$ are calculated and results in (3.14) & (3.15). The duty cycle of the half-bridge inverter Leg c is calculated by substituting (3.14) & (3.15) in (3.11) and is shown in (3.16). The duty cycle d_c is the required duty cycle of the inverter Leg c to reject the ripple current in the dc bus.

$$\hat{V}_z = \frac{n\hat{V}_i}{2}\sqrt{\frac{\hat{Z}|\delta|}{Lf_s}} \tag{3.14}$$

$$\phi_v = \begin{cases} \dfrac{\phi_i + \phi_z}{2}, & \delta > 0 \\ \dfrac{\phi_i + \phi_z + \pi}{2}, & \delta < 0 \end{cases} \tag{3.15}$$

$$d_c(t) = \begin{cases} \frac{1}{2} - \frac{n\hat{V}_i}{2V_d}\sqrt{\frac{\hat{Z}|\delta|}{Lf_s}}\sin\left(\omega_i t + \frac{\phi_i+\phi_z}{2}\right), & \delta > 0 \\ \frac{1}{2} - \frac{n\hat{V}_i}{2V_d}\sqrt{\frac{\hat{Z}|\delta|}{Lf_s}}\sin\left(\omega_i t + \frac{\phi_i+\phi_z+\pi}{2}\right), & \delta < 0 \end{cases} \tag{3.16}$$

3.3 Average modeling of inverter leg currents

Average inverter leg currents i_{lega}, i_{legb}, i_{legc} are derived over a switching cycle T_s with ripple rejection included. The average inverter leg currents are obtained to highlight the unbalance in the inverter leg currents. The modulation inverter comprises of switches S_5, S_6, S_7, S_8 and the ripple rejection inverter comprises of switches S_7, S_8, S_9, S_{10}. Initially, the average inverter leg currents $\bar{i}_{lega,mod}$ & $\bar{i}_{legb,mod}$ are obtained due to the modulation inverter without considering the ripple rejection inverter. Later, the average inverter leg currents $\bar{i}_{legb,rej}$ & $\bar{i}_{legc,rej}$

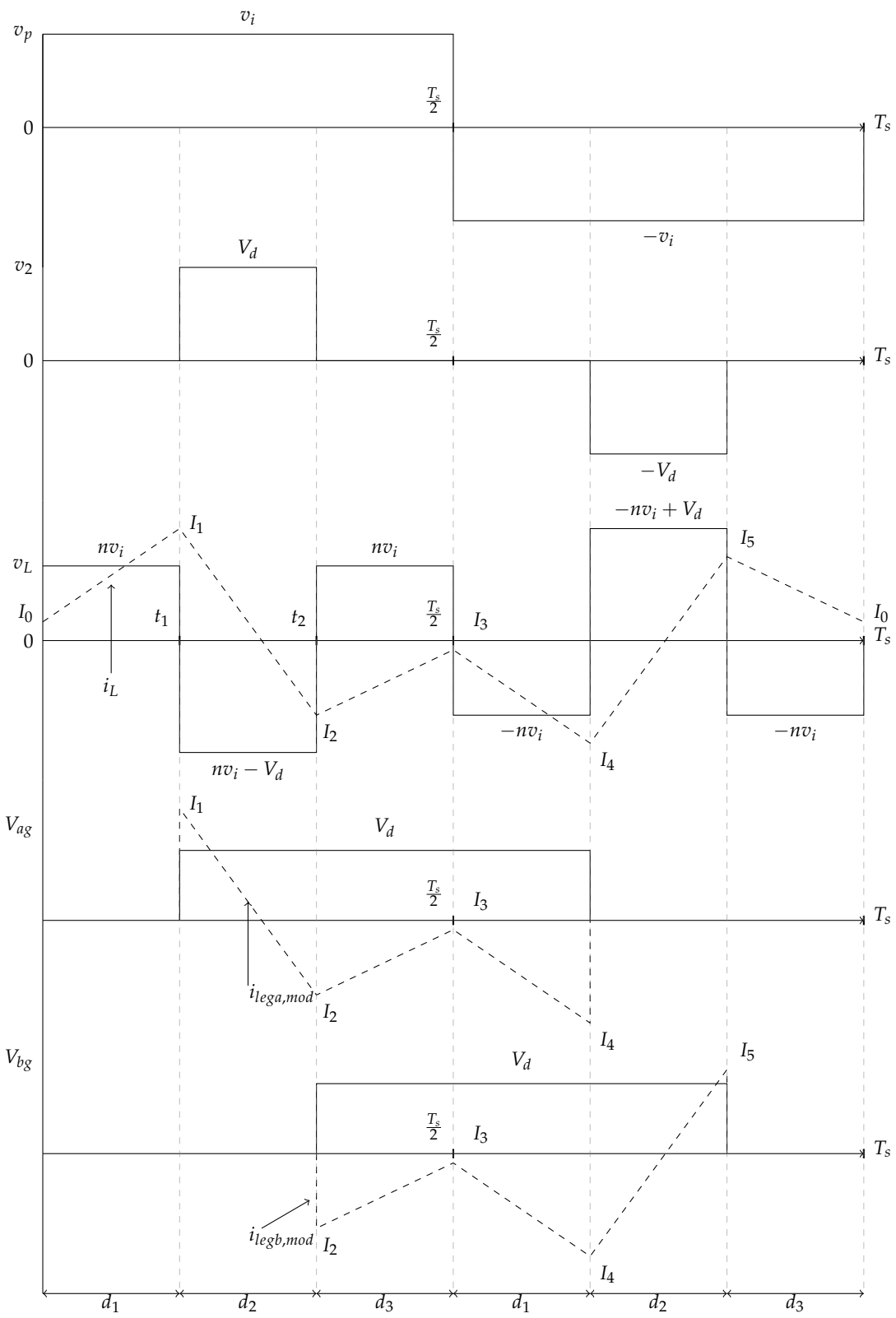

Figure 3.2: Modulation of the single phase bi-directional AC-DC Converter

are obtained solely due to ripple rejection inverter without considering the modulation inverter. Finally, the total average leg currents $\bar{i}_{lega}$, $\bar{i}_{legb}$ & $\bar{i}_{legc}$ are obtained by summing the leg currents due to modulation inverter and rejection inverter.

The average inverter leg currents $\bar{i}_{lega,mod}$ & $\bar{i}_{legb,mod}$ due to the modulation inverter are calculated from the current flowing through the leakage inductance L of the transformer as shown in Fig. 3.2. Current commutation time t_1 & t_2 and duty cycle are calculated from (3.17)-(3.21).

$$t_1 = \frac{T_s}{4}(1 + \delta - |d|) \tag{3.17}$$

$$t_2 = \frac{T_s}{4}(1 + \delta + |d|) \tag{3.18}$$

$$d_1 = \frac{t_1}{T_s/2} = \frac{1}{2}(1 + \delta - |d|) \tag{3.19}$$

$$d_2 = \frac{t_2 - t_1}{T_s/2} = |d| \tag{3.20}$$

$$d_3 = \frac{T_s/2 - t_2}{T_s/2} = \frac{1}{2}(1 - \delta - |d|) \tag{3.21}$$

Assuming 1:1 transformer turns ratio, the transformer leakage inductor current i_L rises from I_0 (3.22) to I_1 (3.23) from time 0 to t_1 with voltage v_i applied to L. During the time t_1 to t_2, the current i_L decrease to I_2 (3.24) with voltage $v_i - V_d$ applied to L. During the time t_2 to $\frac{T_s}{2}$, the current i_L rises to I_3 (3.25) with voltage v_i applied to L. During the time $\frac{T_s}{2}$ to $\frac{T_s}{2} + t_1$, the current i_L decrease to I_4 (3.26) with voltage $-v_i$ applied to L. During the time $\frac{T_s}{2} + t_1$ to $\frac{T_s}{2} + t_2$, the current i_L rises to I_5 (3.27) with voltage $-v_i + V_d$ applied to L. During the time $\frac{T_s}{2} + t_2$ to T_s, the current i_L decreases to I_0 (3.22) with voltage $-v_i$ applied to L.

$$I_0 = \frac{-v_i + dV_d}{4Lf_s} \tag{3.22}$$

$$I_1 = \frac{v_i}{4Lf_s}(1 + \delta - |d|) \tag{3.23}$$

$$I_2 = \frac{1}{4Lf_s}\left[v_i(1 + \delta + |d|) - 2dV_d\right] \tag{3.24}$$

$$I_3 = \frac{1}{2Lf_s}(v_i - dV_d) \tag{3.25}$$

$$I_4 = \frac{1}{4Lf_s}\left[v_i(1 - \delta + |d|) - 2dV_d\right] \tag{3.26}$$

$$I_5 = \frac{1}{4Lf_s}\left[v_i(1 - \delta - |d| - 2d)\right] \tag{3.27}$$

The average inverter leg currents $\bar{i}_{lega,mod}$ & $\bar{i}_{legb,mod}$ due to modulation inverter are calculated by averaging the currents $i_{lega,mod}$ & $i_{legb,mod}$ over a switching cycle T_s. Substituting (3.19) - (3.27) into (3.28) & (3.29) results in the average inverter leg currents $\bar{i}_{lega,mod}$ (3.30) & $\bar{i}_{legb,mod}$ (3.31) due to the modulation inverter.

$$\bar{i}_{lega,mod}(t) = \frac{(I_1 + I_2)\, d_2 + (I_2 + I_3)\, d_3 + (I_3 + I_4)\, d_1 + 2I_0}{4} \tag{3.28}$$

$$\bar{i}_{legb,mod}(t) = \frac{(I_2 + I_3)\, d_3 + (I_3 + I_4)\, d_1 + (I_4 + I_5)\, d_2 + 2I_0}{4} \tag{3.29}$$

$$\bar{i}_{lega,mod}(t) = \frac{1}{16Lf_s}\left[\left(1 - \delta^2 - |d|^2\right) v_i + 2d\left(|d| - 1\right) V_d + 2\delta|d||v_i|\right] \tag{3.30}$$

$$\bar{i}_{legb,mod}(t) = \frac{1}{16Lf_s}\left[\left(1 - \delta^2 - |d|^2\right) v_i + 2d\left(|d| - 1\right) V_d - 2\delta|d||v_i|\right] \tag{3.31}$$

The average inverter leg currents $\bar{i}_{legb,rej}$ (3.32) & $\bar{i}_{legc,rej}$ (3.33) due the ripple rejection inverter are obtained without considering the modulation inverter. The

average inverter leg currents $\bar{i}_{legb,rej}$ & $\bar{i}_{legc,rej}$ are calculated by using d_b, d_c & $\bar{i}_z$ from (3.10), (3.11) & (3.9) and are shown in (3.34) & (3.35).

$$\bar{i}_{legb,rej}(t) = d_b \bar{i}_z(t) \tag{3.32}$$

$$\bar{i}_{legc,rej}(t) = d_c(t)(-i_z(t)) \tag{3.33}$$

$$\bar{i}_{legb,rej}(t) = \frac{\hat{V}_z}{2\hat{Z}} \sin(\omega_i t + \phi_v - \phi_z) \tag{3.34}$$

$$\begin{aligned} \bar{i}_{legc,rej}(t) = &- \frac{\hat{V}_z}{2\hat{Z}} \sin(\omega_i t + \phi_v - \phi_z) + \frac{\hat{V}_z{}^2}{2V_d\hat{Z}} \cos(\phi_z) \\ &- \frac{\hat{V}_z^2}{2V_d\hat{Z}} \cos(2\omega_i t + 2\phi_v - \phi_z) \end{aligned} \tag{3.35}$$

The total average leg currents $\bar{i}_{lega}$, $\bar{i}_{legb}$ & $\bar{i}_{legc}$ (3.36)-(3.38) are obtained by summing the average leg currents due to modulation inverter $\bar{i}_{lega,mod}$ & $\bar{i}_{legb,mod}$ and the average leg currents due to ripple rejection inverter $\bar{i}_{legb,rej}$ & $\bar{i}_{legc,rej}$.

$$\bar{i}_{lega}(t) = \bar{i}_{lega,mod}(t) \tag{3.36}$$

$$\bar{i}_{legb}(t) = \bar{i}_{legb,mod}(t) + \bar{i}_{legb,rej}(t) \tag{3.37}$$

$$\bar{i}_{legc}(t) = \bar{i}_{legc,rej}(t) \tag{3.38}$$

The resulting average leg current profiles are presented in (3.39)-(3.41). It is noteworthy that all the three average leg currents $\bar{i}_{lega}$, $\bar{i}_{legb}$ and $\bar{i}_{legc}$ have distinct current profiles and are unbalanced.

$$\bar{i}_{lega}(t) = \frac{1}{16Lf_s}\left[\left(1-\delta^2-|d|^2\right)v_i + 2d\left(|d|-1\right)V_d + 2\delta|d||v_i|\right] \tag{3.39}$$

$$\bar{i}_{legb}(t) = \frac{1}{16Lf_s}\left[\left(1-\delta^2-|d|^2\right)v_i + 2d\left(|d|-1\right)V_d - 2\delta|d||v_i|\right] + \frac{\hat{V}_z}{2\hat{Z}}\sin(\omega_i t + \phi_v - \phi_z) \tag{3.40}$$

$$\bar{i}_{legc}(t) = -\frac{\hat{V}_z}{2\hat{Z}}\sin(\omega_i t + \phi_v - \phi_z) + \frac{\hat{V}_z^2}{2V_d\hat{Z}}\cos(\phi_z) - \frac{\hat{V}_z^2}{2V_d\hat{Z}}\cos(2\omega_i t + 2\phi_v - \phi_z) \tag{3.41}$$

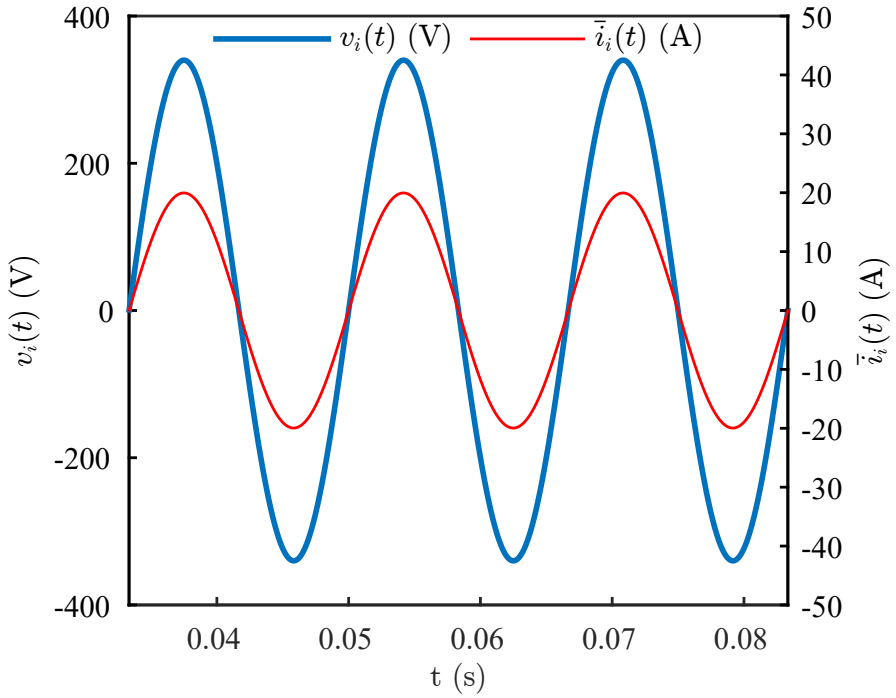

Figure 3.3: Simulation results: $v_i(t)$, $\bar{i}_i(t)$ with $\delta = 0.1647$, $\phi_i = 0$ rad

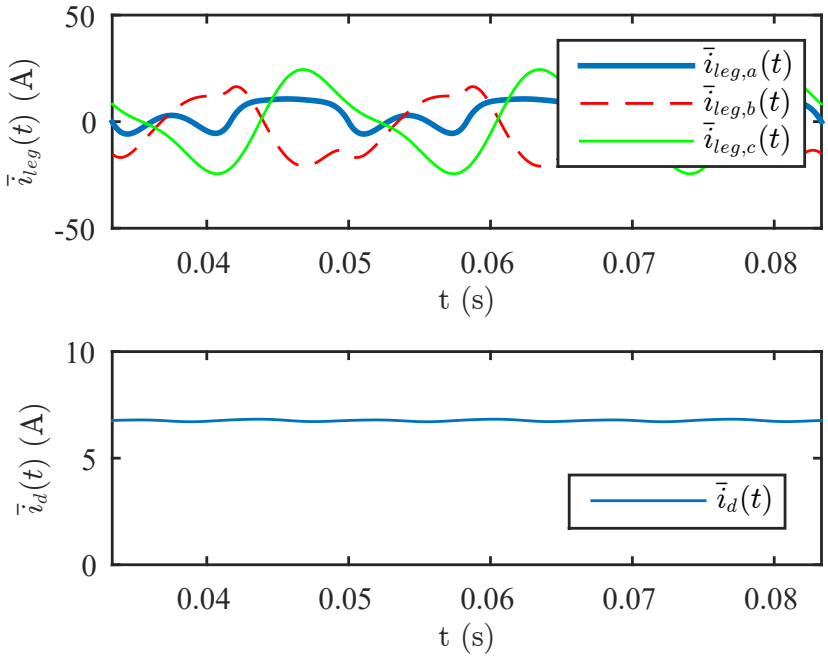

Figure 3.4: Simulation results: $\bar{i}_{leg}(t)$, $\bar{i}_d(t)$ with $\delta = 0.1647$, $\phi_i = 0$ rad

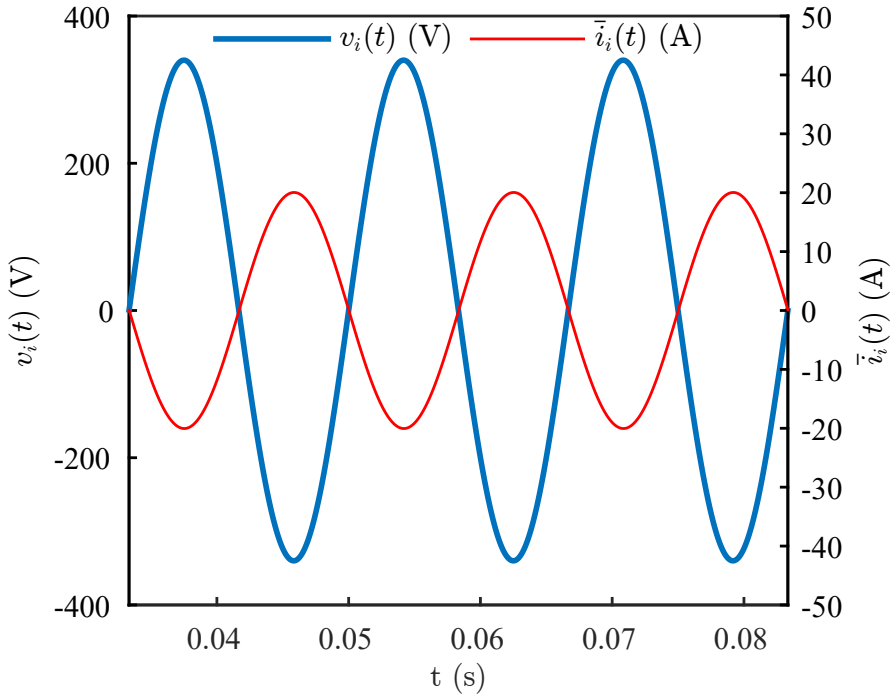

Figure 3.5: Simulation results: $v_i(t)$, $\bar{i}_i(t)$ with δ = -0.1647, ϕ_i = 0 rad

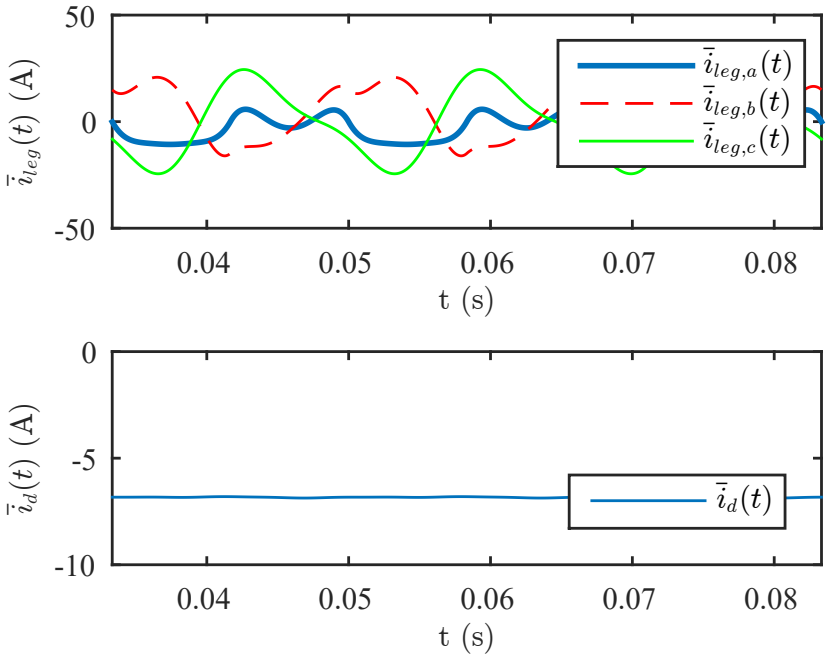

Figure 3.6: Simulation results: $\bar{i}_{leg}(t)$, $\bar{i}_d(t)$ with δ = -0.1647, ϕ_i = 0 rad

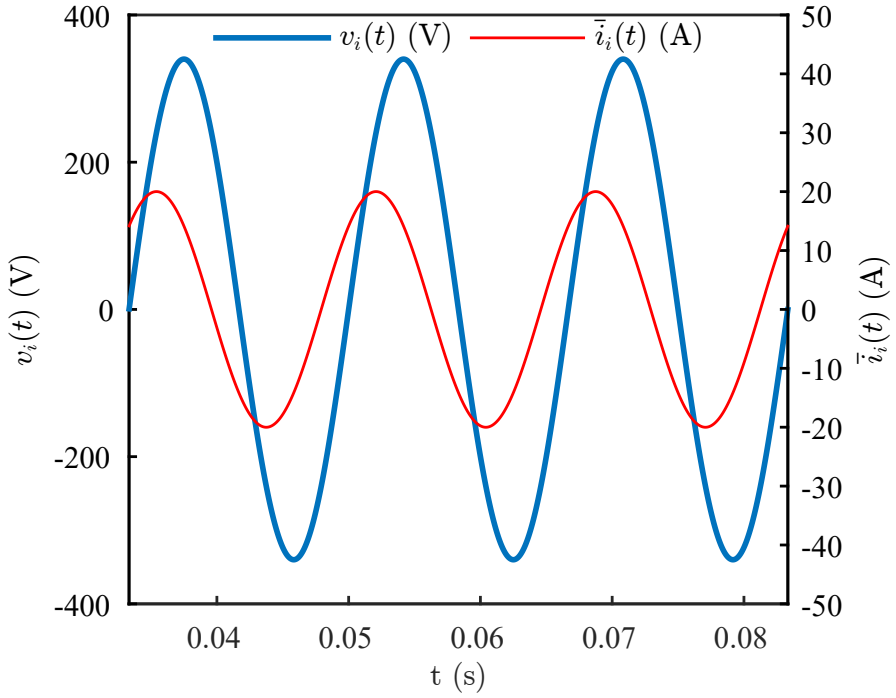

Figure 3.7: Simulation results: $v_i(t)$, $\bar{i}_i(t)$ with $\delta = 0.1647$, $\phi_i = \frac{\pi}{4}$ rad

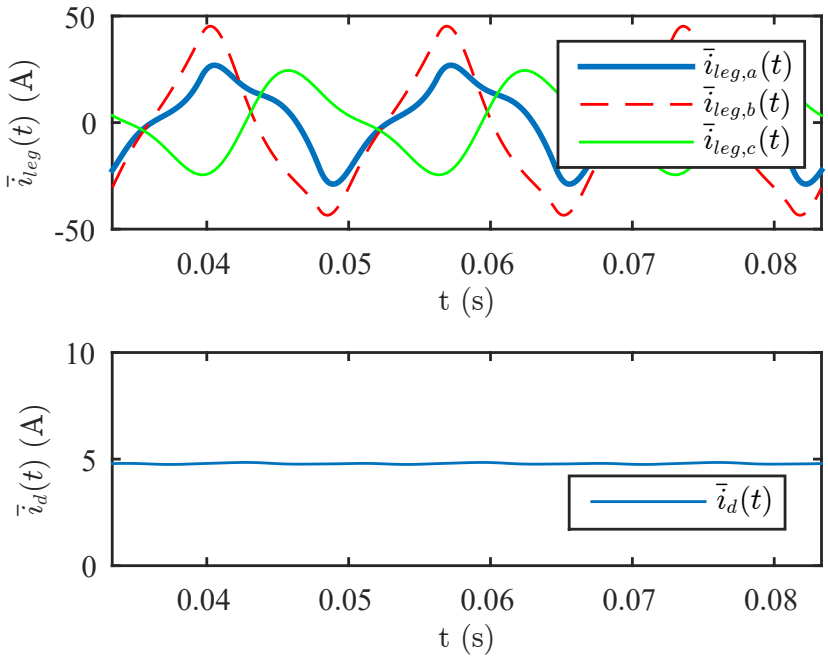

Figure 3.8: Simulation results: $\bar{i}_{leg}(t)$, $\bar{i}_d(t)$ with $\delta = 0.1647$, $\phi_i = \frac{\pi}{4}$ rad

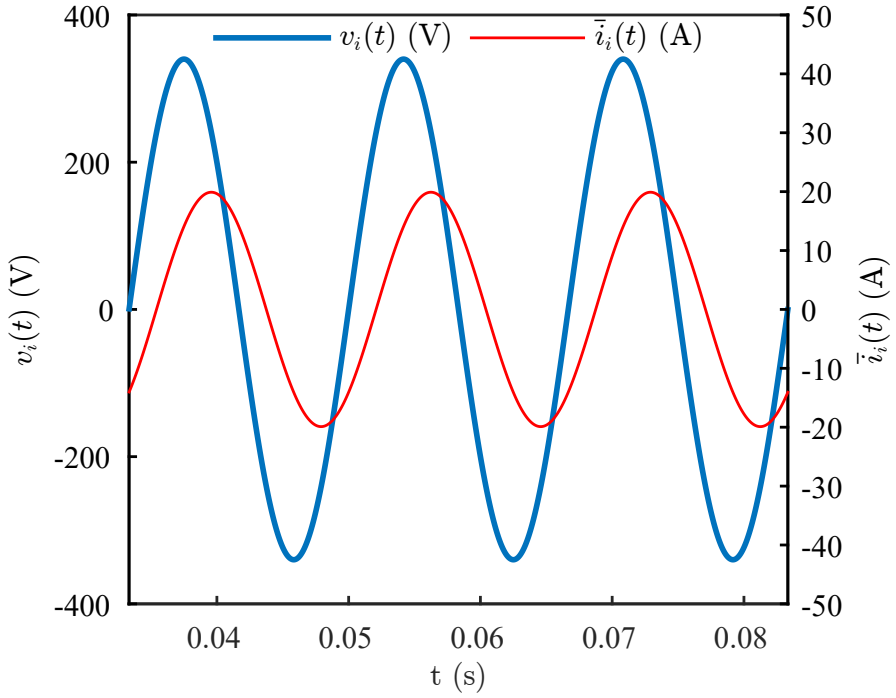

Figure 3.9: Simulation results: $v_i(t)$, $\bar{i}_i(t)$ with $\delta = 0.1647$, $\phi_i = -\frac{\pi}{4}$ rad

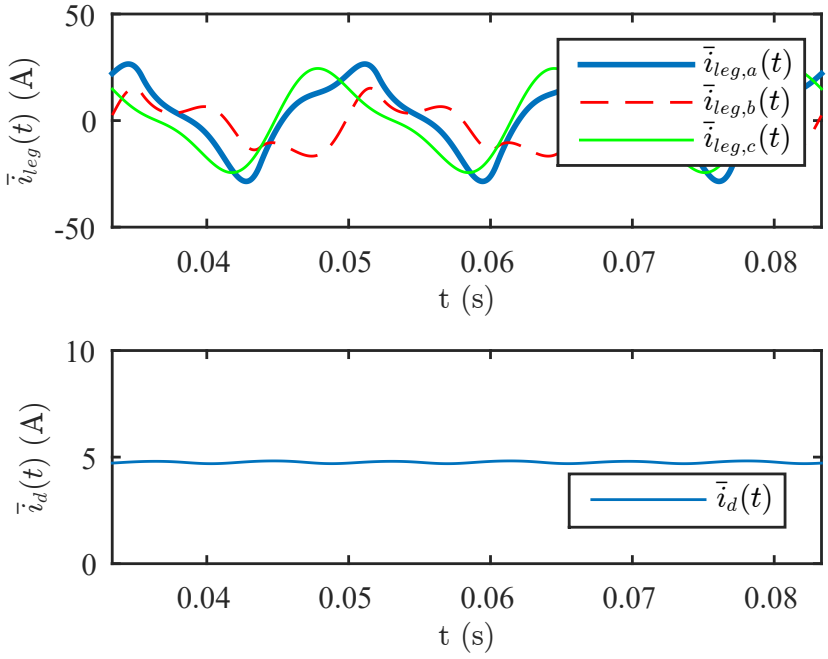

Figure 3.10: Simulation results: $\bar{i}_{leg}(t)$, $\bar{i}_d(t)$ with $\delta = 0.1647$, $\phi_i = -\frac{\pi}{4}$ rad

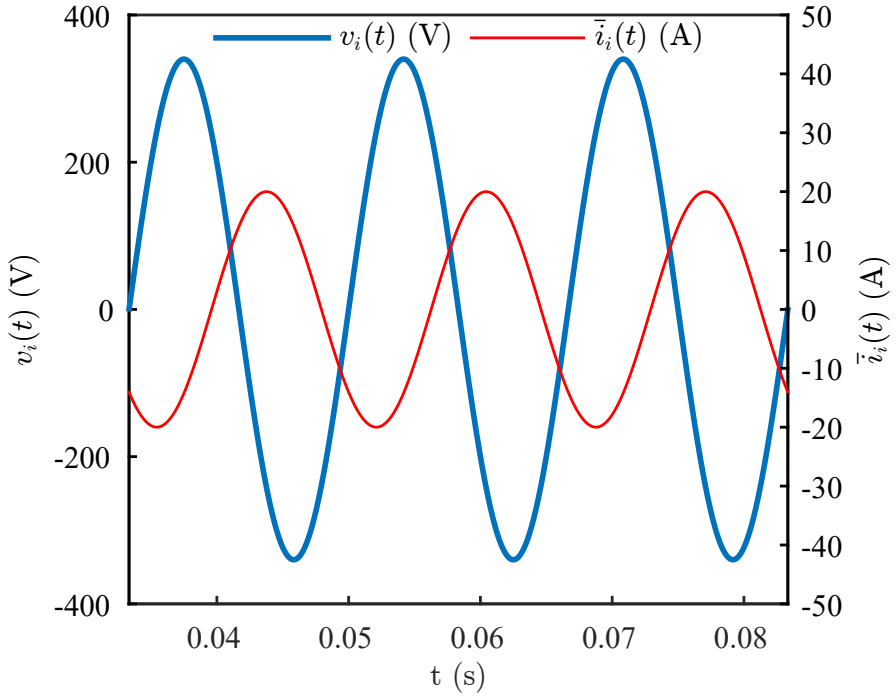

Figure 3.11: Simulation results: $v_i(t)$, $\bar{i}_i(t)$ with δ = -0.1647, $\phi_i = \frac{\pi}{4}$ rad

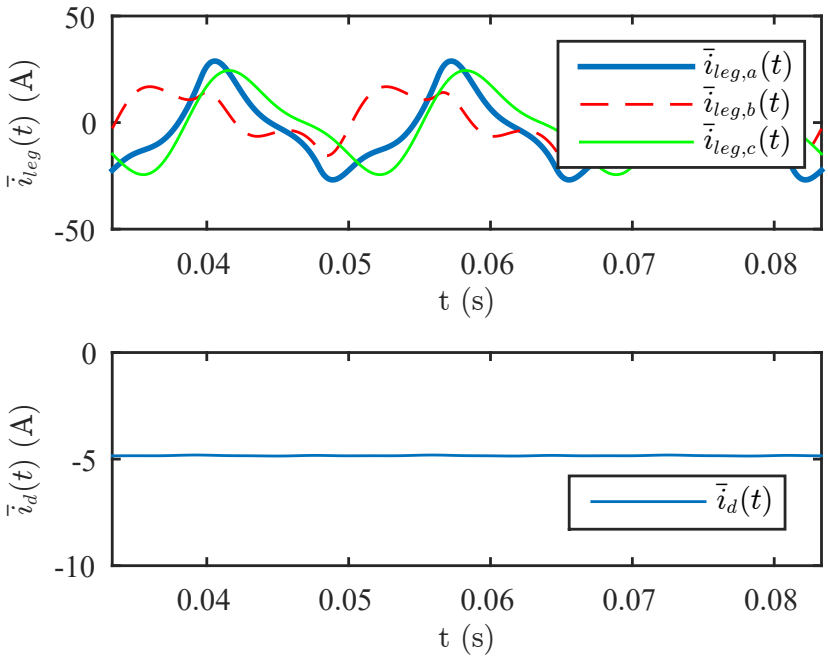

Figure 3.12: Simulation results: $\bar{i}_{leg}(t)$, $\bar{i}_d(t)$ with δ = -0.1647, $\phi_i = \frac{\pi}{4}$ rad

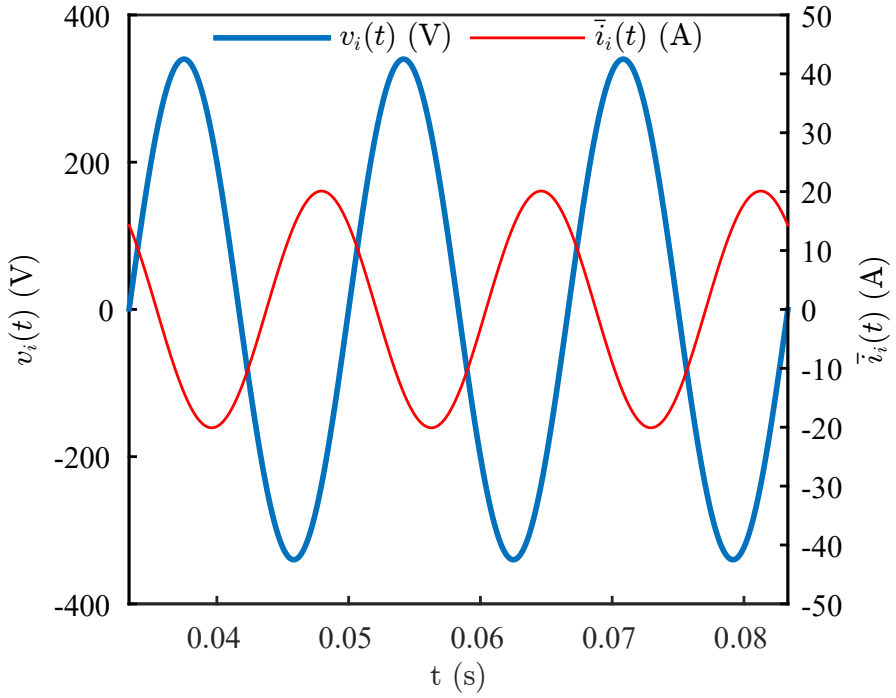

Figure 3.13: Simulation results: $v_i(t)$, $\bar{i}_i(t)$ with δ = -0.1647, ϕ_i = -$\frac{\pi}{4}$ rad

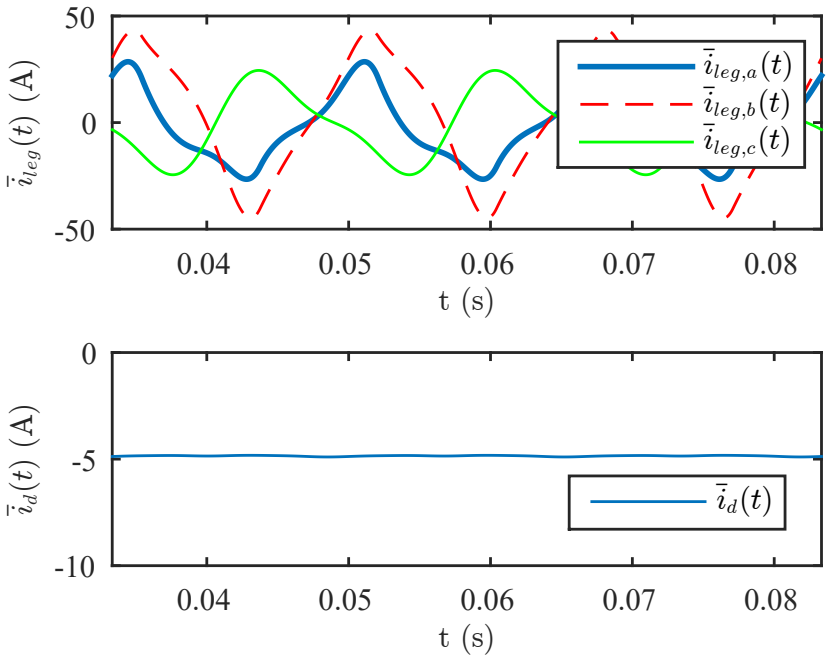

Figure 3.14: Simulation results: $\bar{i}_{leg}(t)$, $\bar{i}_d(t)$ with δ = -0.1647, ϕ_i = -$\frac{\pi}{4}$ rad

Table 3.1: Simulation setup of a single phase bi-directional AC-DC converter with ripple rejection

L	$\hat{V}_i$	w_i	f_s	V_d	R_z	L_z
$7\mu H$	$240\sqrt{2}V$	$2\pi 60\ \frac{rad}{s}$	$100kHz$	$500V$	0.1Ω	$0.01H$

3.4 Simulation

The topology shown in Fig. 3.1 is simulated in PLECS with the conditions shown in Table 3.1. All the switches and diodes used are assumed to be ideal. The single phase matrix converter is operated with a fixed duty cycle of 50% at 100 kHz. The matrix converter applies v_i for the first 5μs interval and then applies $-v_i$ for the next 5μs interval. The half-bridge leg a and leg b operate at a fixed 50% duty cycle with phase shift modulation [22]. The magnitude $\hat{V}_z$ and the phase angle ϕ_v are calculated from (3.14), (3.15) and the half-bridge inverter leg c is operated with duty cycle d_c (3.16). Various operating conditions at different δ and ϕ_i are simulated in order to confirm ripple current rejection in the DC bus.

The simulation results in Fig. 3.3 & 3.4 illustrate active power transfer from the AC grid to the DC bus with $\delta = 0.1647$ and $\phi_i = 0\ rad$. The input voltage, input current, average leg currents, and average dc bus current are shown in Fig. 3.3 and 3.4. In this case, the battery charger acts like a resistive load consuming active power from the AC grid.

The simulation results in Fig. 3.5 & 3.6 display active power transfer from the DC bus to the AC grid with $\delta = -0.1647$ and $\phi_i = 0\ rad$. The input voltage, input current, average leg currents, and average dc bus current are shown in Fig. 3.5 & 3.6. In this case, the battery charger acts like an ideal generator to supply active power to the AC grid.

The simulation results in Fig. 3.7 & 3.8 depict active power transfer from the AC grid to the DC bus and reactive power supplied to the AC grid with $\delta = 0.1647$ and $\phi_i = \frac{\pi}{4}\ rad$. The input voltage, input current, average leg currents, and average dc bus current are shown in Fig. 3.7 & 3.8. In this case, the battery charger acts like a capacitive load to consume active power from the AC grid and supply reactive power to the AC grid.

The simulation results in Fig. 3.9 & 3.10 present active power transfer from the AC grid to the DC bus and reactive power supplied by the AC grid with $\delta = 0.1647$ and $\phi_i = -\frac{\pi}{4}\ rad$. The input voltage, input current, average leg currents, and average dc bus current are shown in Fig. 3.9 & 3.10. In this case, the battery charger acts like an inductive load to consume active power from the AC grid and consume reactive power from the AC grid.

The simulation results in Fig. 3.11 & 3.12 show active power transfer from the DC bus to the AC grid and reactive power supplied to the AC grid with $\delta = -0.1647$ and $\phi_i = \frac{\pi}{4}\ rad$. The input voltage, input current, average leg currents, and average dc bus current are shown in Fig. 3.11 & 3.12. In this case, the battery charger acts like an over excited synchronous generator to generate active power and supply reactive power to the AC grid.

The simulation results in Fig. 3.13 & 3.14 show active power transfer from the DC bus to the AC grid and reactive power supplied by the AC grid with $\delta = -0.1647$ and $\phi_i = -\frac{\pi}{4}\ rad$. The input voltage, input current, average leg currents, and average dc bus current are shown in Fig. 3.13 & 3.14. In this case, the battery charger acts like an under excited synchronous generator to generate active power and consume reactive power from the AC grid.

The average dc bus current at various operating conditions is mostly DC while the average leg currents have distinct current profiles and are unbalanced.

CHAPTER 4

THREE PHASE BI-DIRECTIONAL SIC AC-DC CONVERTER

4.1 Introduction

A bi-directional battery charger capable of sinking or sourcing real or reactive power with V2G functionality is presented in [15–21]. A bi-directional three phase AC-DC converter with complex closed loop control was proposed in [7] which adds significant line frequency harmonics to the input current. A new modulation strategy was proposed in [12] which overcame the problems in [7], however, it lacks closed loop control. In this chapter, a DQ current control to sink or source real and reactive power in the AC grid is presented. The modulation of the three phase bi-directional AC-DC converter is discussed. Simulation results are are shown to verify the analysis.

4.2 Analysis

DQ current control of the Dual Active Bridge (DAB) based three phase AC-DC converter is briefly analyzed in this section. The converter shown in Fig. 4.1 consists of a LC filter circuit to filter input current harmonics. The source phase voltages $v_a(t)$, $v_b(t)$, $v_c(t)$ with an angular frequency ω_i are shown in (4.1).

$$\begin{aligned} v_a(t) &= \hat{V}\cos(w_i t) \\ v_b(t) &= \hat{V}\cos(w_i t - \frac{2\pi}{3}) \\ v_c(t) &= \hat{V}\cos(w_i t - \frac{4\pi}{3}) \end{aligned} \tag{4.1}$$

The voltage drop across the filter inductor is assumed negligible, therefore the matrix converter phase voltages $v_{ma}(t)$, $v_{mb}(t)$, $v_{mc}(t)$ are approximately equal to the source phase voltages $v_a(t)$, $v_b(t)$, $v_c(t)$ (4.2).

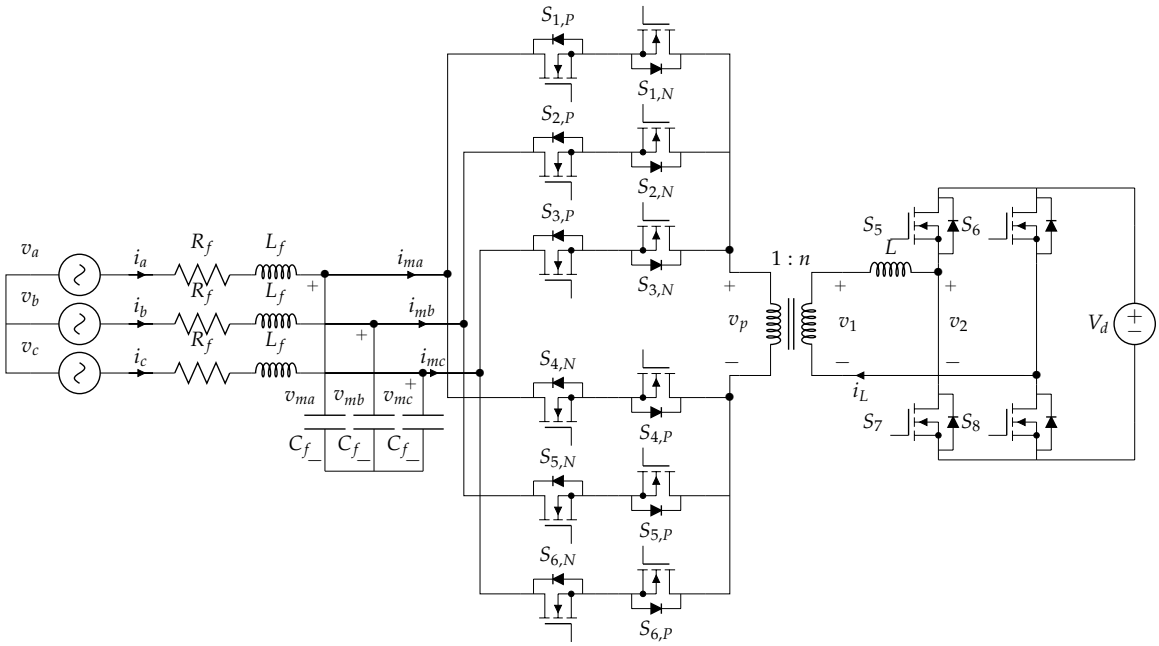

Figure 4.1: Three phase bi-directional AC-DC Converter topology

$$
\begin{aligned}
v_{ma}(t) &= \hat{V}_m \cos(w_i t) \\
v_{mb}(t) &= \hat{V}_m \cos(w_i t - \frac{2\pi}{3}) \\
v_{mc}(t) &= \hat{V}_m \cos(w_i t - \frac{4\pi}{3})
\end{aligned}
\tag{4.2}
$$

The average matrix converter currents $i_{ma}(t)$, $i_{mb}(t)$, $i_{mc}(t)$ are related to the duty cycles $d_a(t)$, $d_b(t)$, $d_c(t)$ (4.3) respectively as shown in (4.4). An additional controllable phase angle ϕ_m is added to control the angle of $i_m(t)$ as shown in (4.5).

$$
\begin{aligned}
d_a(t) &= \frac{|v_{ab}(t)|\, n}{V_d} \\
d_b(t) &= \frac{|v_{bc}(t)|\, n}{V_d} \\
d_c(t) &= \frac{|v_{ca}(t)|\, n}{V_d}
\end{aligned}
\tag{4.3}
$$

$$\begin{aligned}
\bar{i}_{ma}(t) &= \frac{n\delta V_d}{4Lf_s} d_a(t) \\
\bar{i}_{mb}(t) &= \frac{n\delta V_d}{4Lf_s} d_b(t) \\
\bar{i}_{mc}(t) &= \frac{n\delta V_d}{4Lf_s} d_c(t)
\end{aligned} \tag{4.4}$$

By substituting (4.5) in (4.4), the average currents $\bar{i}_{ma}(t)$, $\bar{i}_{mb}(t)$, $\bar{i}_{mc}(t)$ are shown in (4.7) with a constant gain K_b (4.6). The variables δ and ϕ_m control the magnitude and angle of $\bar{i}_{ma}(t)$, $\bar{i}_{mb}(t)$, $\bar{i}_{mc}(t)$ respectively.

$$\begin{aligned}
d_a(t) &= \frac{\sqrt{3}\left|\hat{V}_m \cos(w_i t + \frac{\pi}{6} + \phi_m)\right| n}{V_d} \\
d_b(t) &= \frac{\sqrt{3}\left|\hat{V}_m \cos(w_i t - \frac{\pi}{2} + \phi_m)\right| n}{V_d} \\
d_c(t) &= \frac{\sqrt{3}\left|\hat{V}_m \cos(w_i t - \frac{7\pi}{6} + \phi_m)\right| n}{V_d}
\end{aligned} \tag{4.5}$$

$$K_b = \frac{n^2 \hat{V}_m}{4Lf_s} \tag{4.6}$$

$$\begin{aligned}
\bar{i}_{ma}(t) &= K_b \delta \cos(w_i t + \phi_m) \\
\bar{i}_{mb}(t) &= K_b \delta \cos(w_i t - \frac{2\pi}{3} + \phi_m) \\
\bar{i}_{mc}(t) &= K_b \delta \cos(w_i t - \frac{4\pi}{3} + \phi_m)
\end{aligned} \tag{4.7}$$

A relation between the average matrix converter currents $i_{ma}(t)$, $i_{mb}(t)$, $i_{mc}(t)$ are expressed in terms of the source currents $i_a(t)$, $i_b(t)$, $i_c(t)$ with the LC filter circuit in (4.8) respectively. The equation shown in (4.9) is used to transform a three phase signal into two dc quantities in a rotating reference frame with θ rad. The control variables are now dc values which is easier to control.

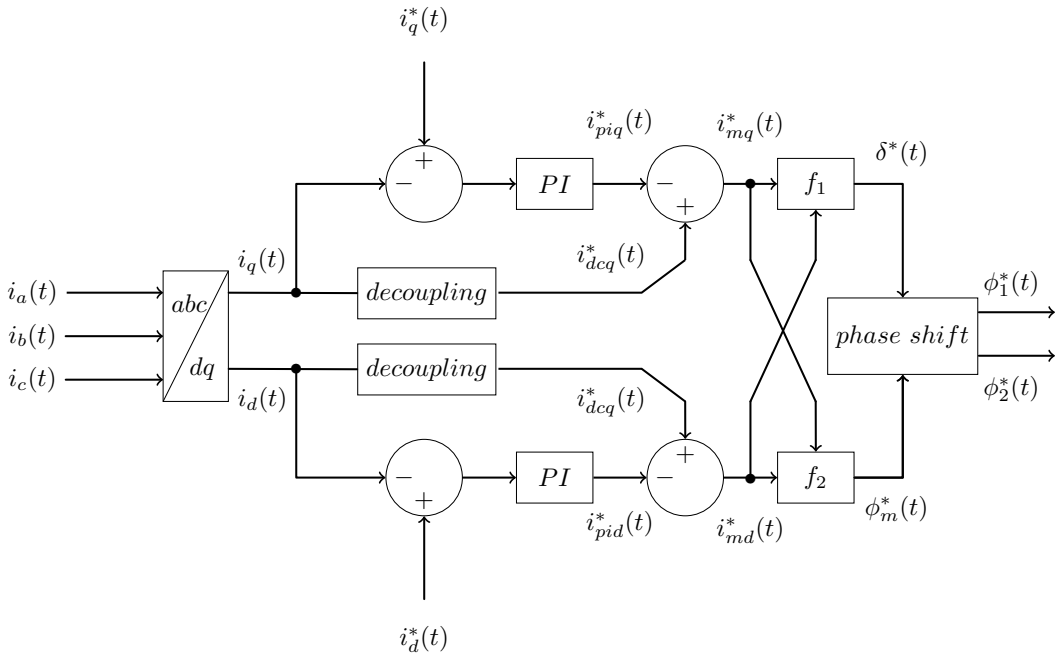

Figure 4.2: Control diagram of a three phase bi-directional AC-DC converter

$$
\begin{aligned}
i_{ma}(t) &= L_f C_f \frac{\mathrm{d}^2}{\mathrm{dt}^2} i_a(t) + R_f C_f \frac{\mathrm{d}}{\mathrm{dt}} i_a(t) + i_a(t) - C_f \frac{\mathrm{d}}{\mathrm{dt}} v_a(t) \\
i_{mb}(t) &= L_f C_f \frac{\mathrm{d}^2}{\mathrm{dt}^2} i_b(t) + R_f C_f \frac{\mathrm{d}}{\mathrm{dt}} i_b(t) + i_b(t) - C_f \frac{\mathrm{d}}{\mathrm{dt}} v_b(t) \\
i_{mc}(t) &= L_f C_f \frac{\mathrm{d}^2}{\mathrm{dt}^2} i_c(t) + R_f C_f \frac{\mathrm{d}}{\mathrm{dt}} i_c(t) + i_c(t) - C_f \frac{\mathrm{d}}{\mathrm{dt}} v_c(t)
\end{aligned} \tag{4.8}
$$

$$
\begin{pmatrix} y_d \\ y_q \end{pmatrix} = \begin{pmatrix} \cos\theta & \cos(\theta - \frac{2\pi}{3}) & \cos(\theta + \frac{2\pi}{3}) \\ -\sin\theta & -\sin(\theta - \frac{2\pi}{3}) & -\sin(\theta + \frac{2\pi}{3}) \end{pmatrix} \begin{pmatrix} x_a \\ x_b \\ x_c \end{pmatrix} \tag{4.9}
$$

Proportional-Integral (PI) controllers are implemented to track the reference currents $i_d^*(t)$ & $i_q^*(t)$ with the actual currents $i_d(t)$ & $i_q(t)$. The steady state error between the reference and the actual currents are driven to zero. The equations (4.10) & (4.11) are the PI controller responses $i_{pid}^*(t)$ & $i_{piq}^*(t)$.

$$
{i_{pid}}^*(t) = K_p \left({i_d}^*(t) - i_d(t) \right) + K_i \int \left({i_d}^*(t) - i_d(t) \right) dt \tag{4.10}
$$

Table 4.1: Simulation setup of a three phase bi-directional AC-DC converter

$\hat{V}$	ω_i	f_s	V_d	L_f	C_f	L
$120\sqrt{2}V$	$2\pi 60\ \frac{rad}{s}$	$33.33kHz$	$500V$	$100\mu H$	$30\mu F$	$7\mu H$

$$i_{piq}{}^*(t) = K_p\left(i_q{}^*(t) - i_q(t)\right) + K_i\int\left(i_q{}^*(t) - i_q(t)\right)dt \tag{4.11}$$

The control variables $\delta^*(t)$ & $\phi^*(t)$ can be calculated from the reference currents $i^*_{md}(t)$ & $i^*_{mq}(t)$ as shown in (4.12) & (4.13).

$$\delta^*(t) = \text{sgn}(i_{md}{}^*(t))\frac{1}{K_b}\sqrt{i_{md}{}^*(t)^2 + i_{mq}{}^*(t)^2} \tag{4.12}$$

$$\phi^*_m(t) = \tan^{-1}\left(\frac{i_{mq}{}^*(t)}{i_{md}{}^*(t)}\right) \tag{4.13}$$

The duty cycle of the half bridges (S_5, S_7) and (S_6, S_8) are fixed at 50%. The phase shift of the half bridges (S_5, S_7) and (S_6, S_8) are $\phi^*_1(t)$ and $\phi^*_2(t)$ and are calculated from (4.14), (4.15) and (4.16).

$$\begin{aligned}
\phi^*_{a1}(t) &= \frac{\pi}{2}\left[\frac{\sqrt{3}n\hat{V}_m}{V_d}\cos(w_i t + \frac{\pi}{6} + \phi^*_m(t)) + \delta^*(t)\right] \\
\phi^*_{a2}(t) &= \frac{\pi}{2}\left[-\frac{\sqrt{3}n\hat{V}_m}{V_d}\cos(w_i t + \frac{\pi}{6} + \phi^*_m(t)) + \delta^*(t)\right]
\end{aligned} \tag{4.14}$$

$$\begin{aligned}
\phi^*_{b1}(t) &= \frac{\pi}{2}\left[\frac{\sqrt{3}n\hat{V}_m}{V_d}\cos(w_i t - \frac{\pi}{2} + \phi^*_m(t)) + \delta^*(t)\right] \\
\phi^*_{b2}(t) &= \frac{\pi}{2}\left[-\frac{\sqrt{3}n\hat{V}_m}{V_d}\cos(w_i t - \frac{\pi}{2} + \phi^*_m(t)) + \delta^*(t)\right]
\end{aligned} \tag{4.15}$$

$$\begin{aligned}
\phi^*_{c1}(t) &= \frac{\pi}{2}\left[\frac{\sqrt{3}n\hat{V}_m}{V_d}\cos(w_i t - \frac{7\pi}{6} + \phi^*_m(t)) + \delta^*(t)\right] \\
\phi^*_{c2}(t) &= \frac{\pi}{2}\left[-\frac{\sqrt{3}n\hat{V}_m}{V_d}\cos(w_i t - \frac{7\pi}{6} + \phi^*_m(t)) + \delta^*(t)\right]
\end{aligned} \tag{4.16}$$

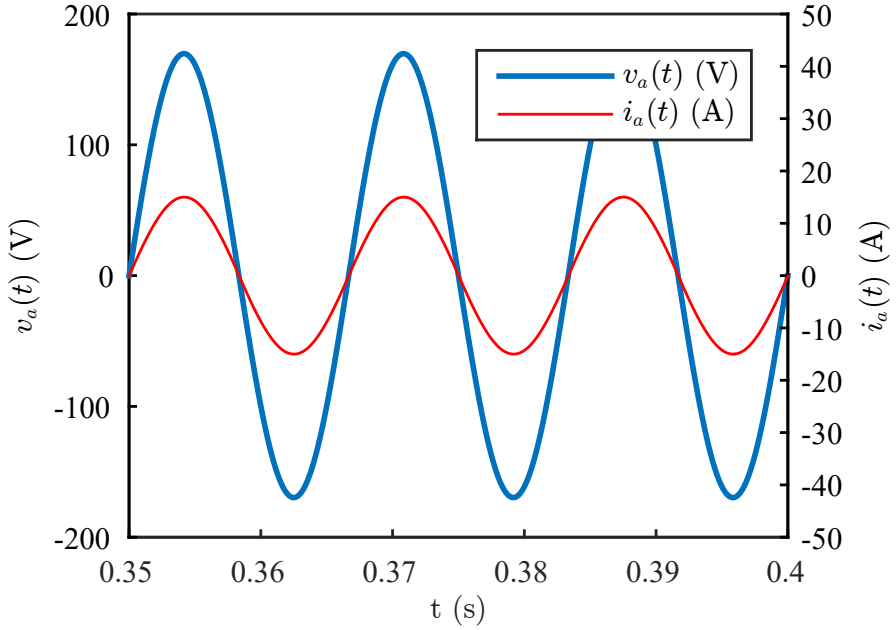

Figure 4.3: Simulation results: $v_a(t)$ & $i_a(t)$ for (i_d, i_q) = (15,0) A

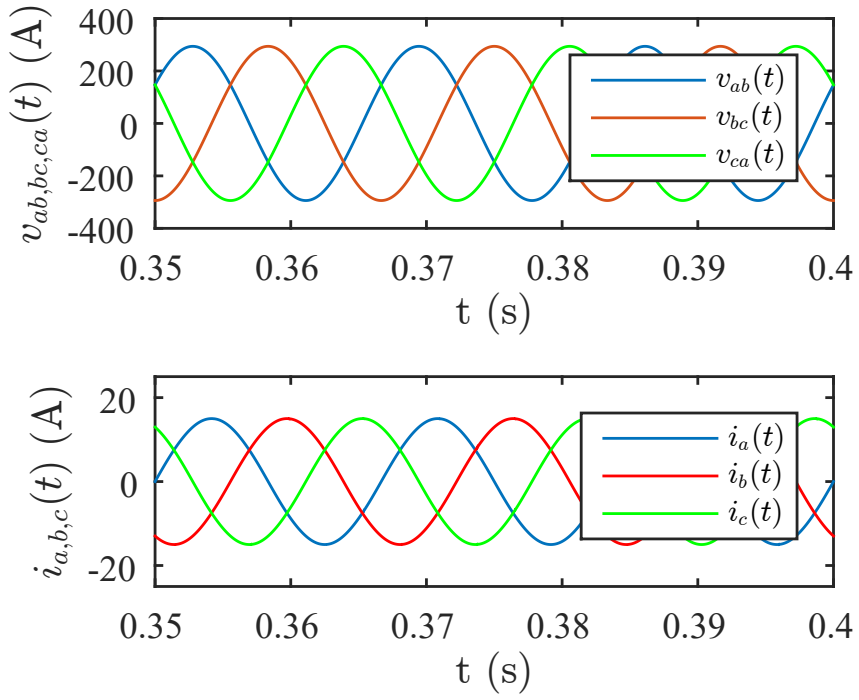

Figure 4.4: Simulation results: $v_{ab,bc,ca}(t)$ & $i_{a,b,c}(t)$ for (i_d, i_q) = (15,0) A

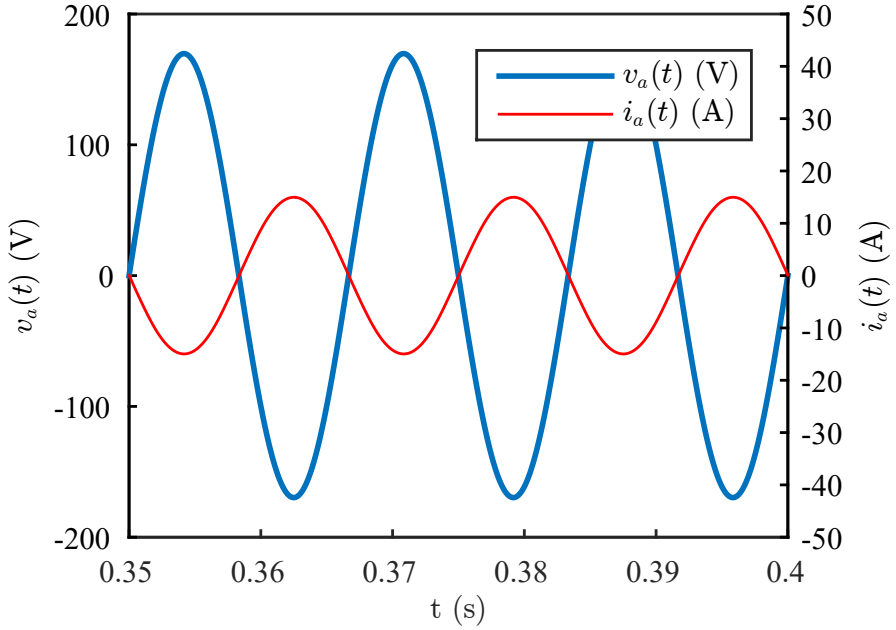

Figure 4.5: Simulation results: $v_a(t)$ & $i_a(t)$ for (i_d, i_q) = (-15,0) A

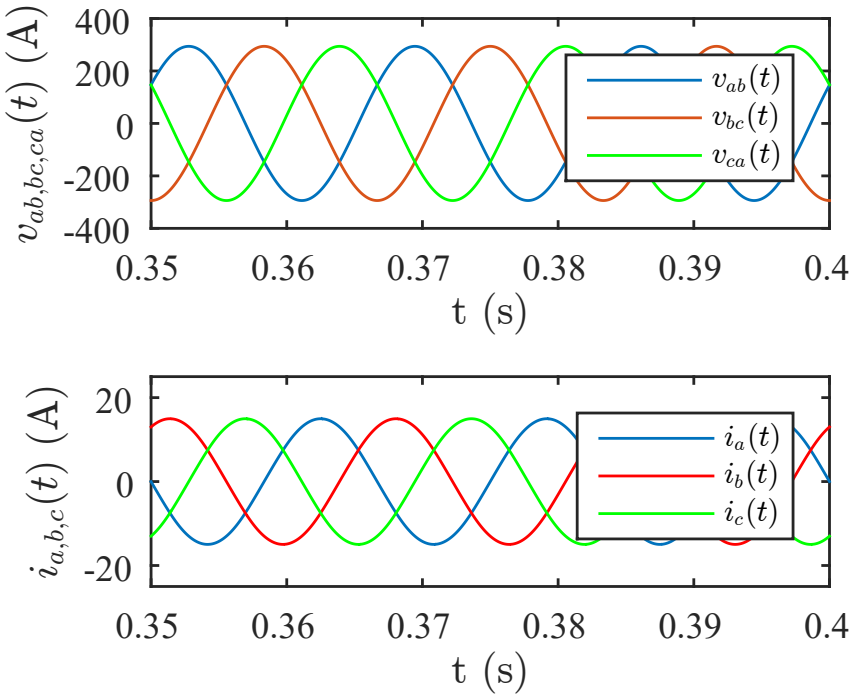

Figure 4.6: Simulation results: $v_{ab,bc,ca}(t)$ & $i_{a,b,c}(t)$ for (i_d, i_q) = (-15,0) A

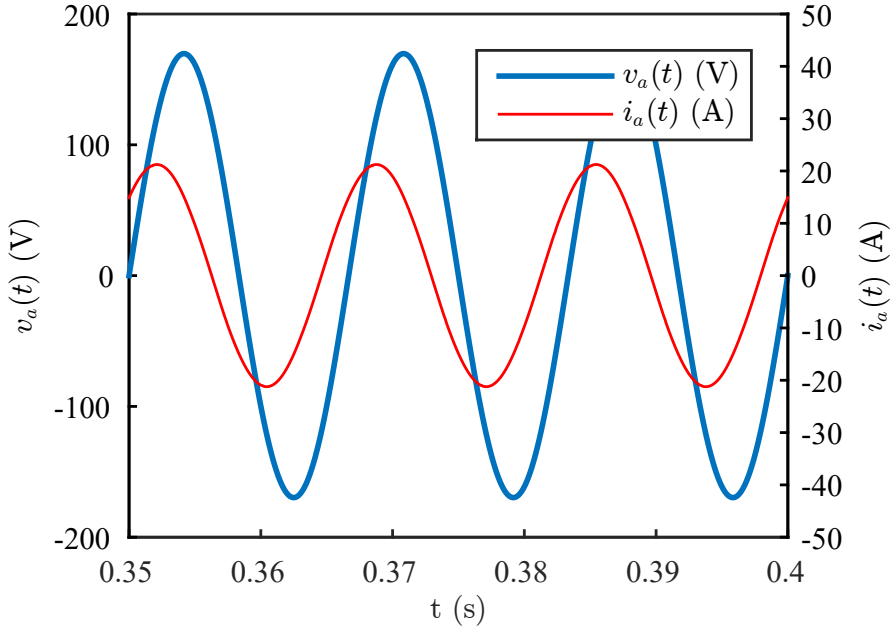

Figure 4.7: Simulation results: $v_a(t)$ & $i_a(t)$ for (i_d, i_q) = (15,15) A

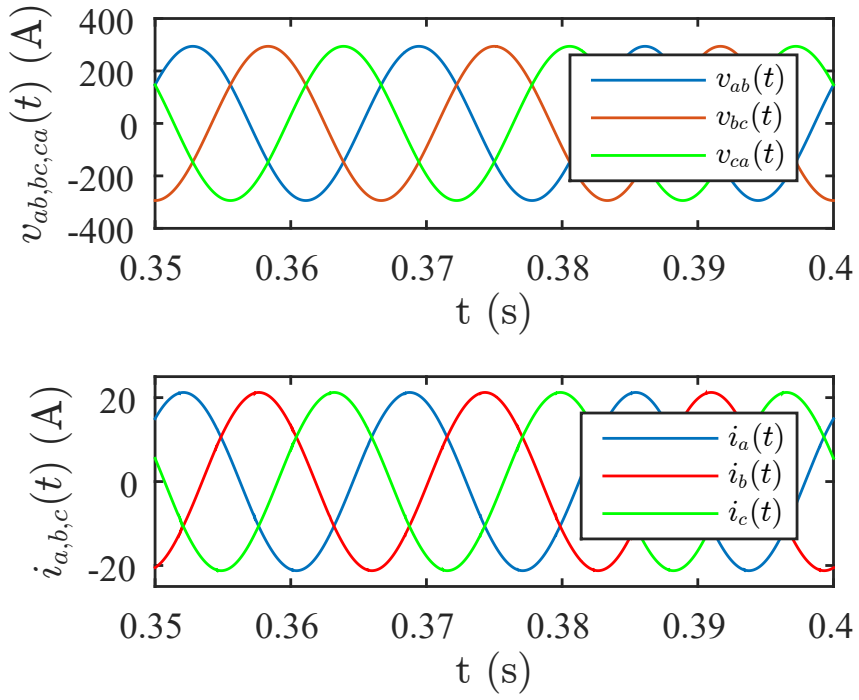

Figure 4.8: Simulation results: $v_{ab,bc,ca}(t)$ & $i_{a,b,c}(t)$ for (i_d, i_q) = (15,15) A

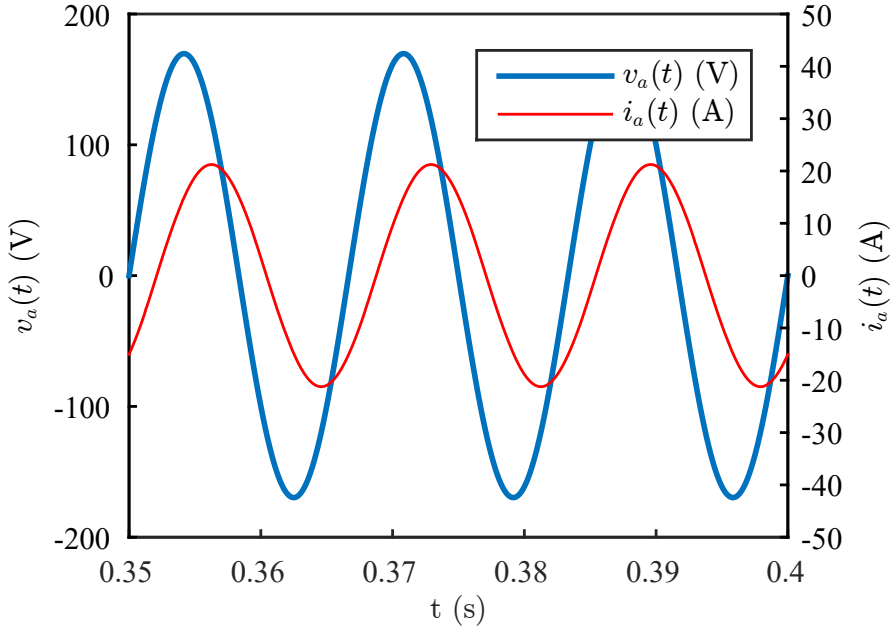

Figure 4.9: Simulation results: $v_a(t)$ & $i_a(t)$ for (i_d, i_q) = (15,-15) A

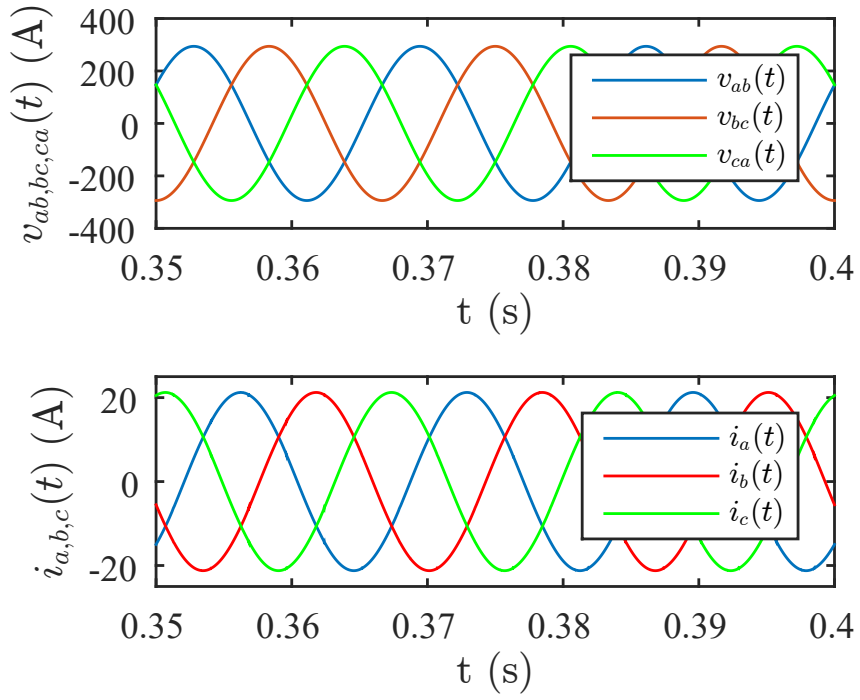

Figure 4.10: Simulation results: $v_{ab,bc,ca}(t)$ & $i_{a,b,c}(t)$ for (i_d, i_q) = (15,-15) A

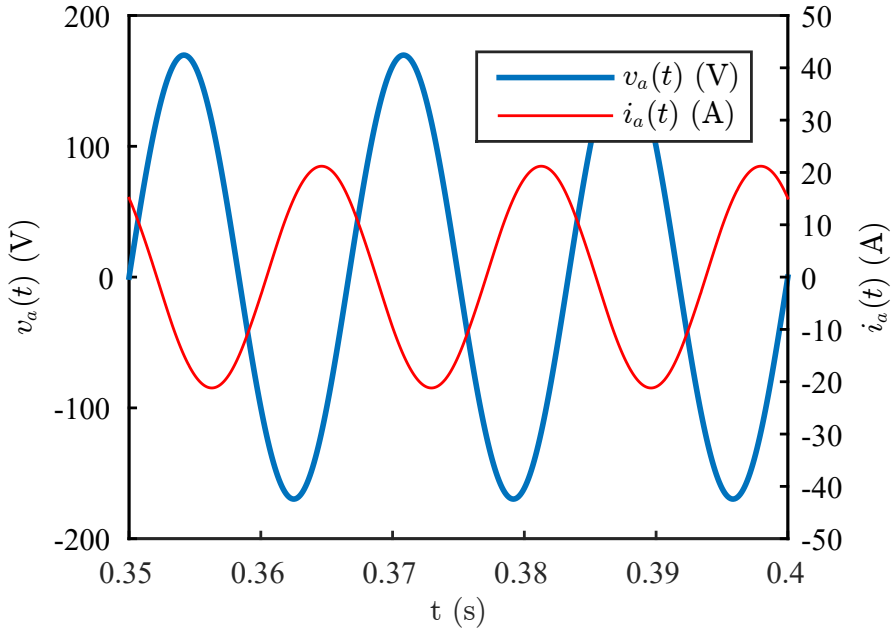

Figure 4.11: Simulation results: $v_a(t)$ & $i_a(t)$ for (i_d, i_q) = (-15,15) A

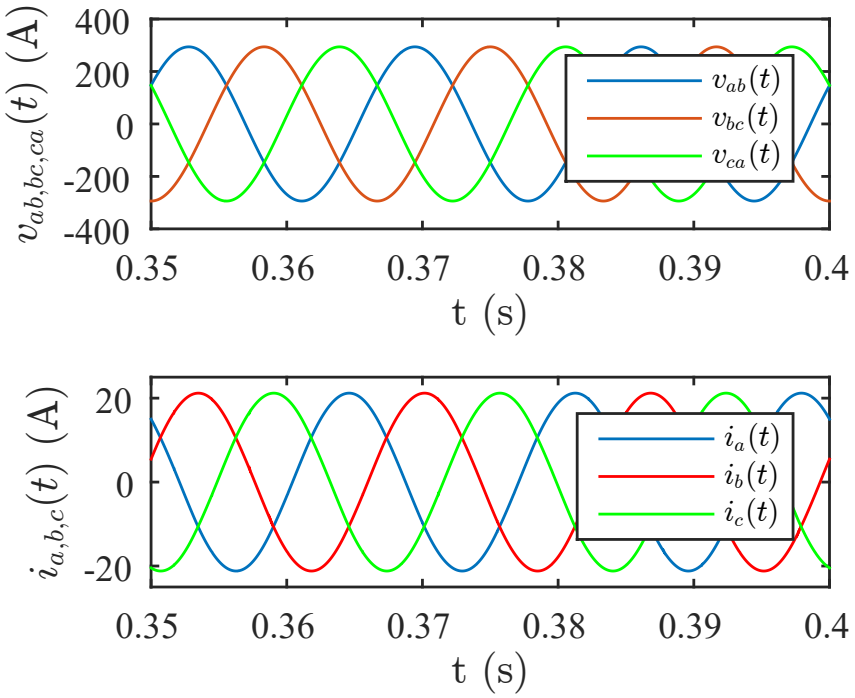

Figure 4.12: Simulation results: $v_{ab,bc,ca}(t)$ & $i_{a,b,c}(t)$ for (i_d, i_q) = (-15,15) A

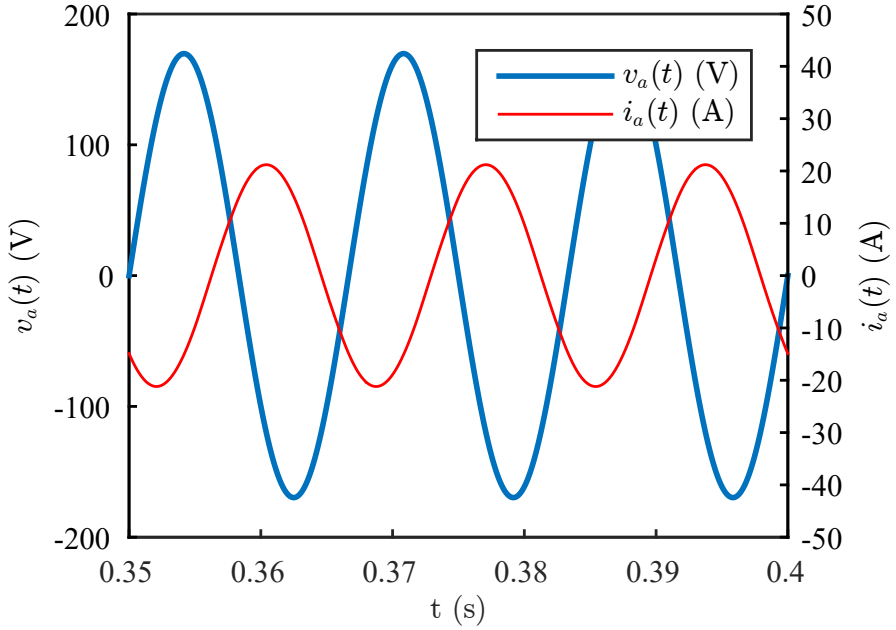

Figure 4.13: Simulation results: $v_a(t)$ & $i_a(t)$ for (i_d, i_q) = (-15,-15) A

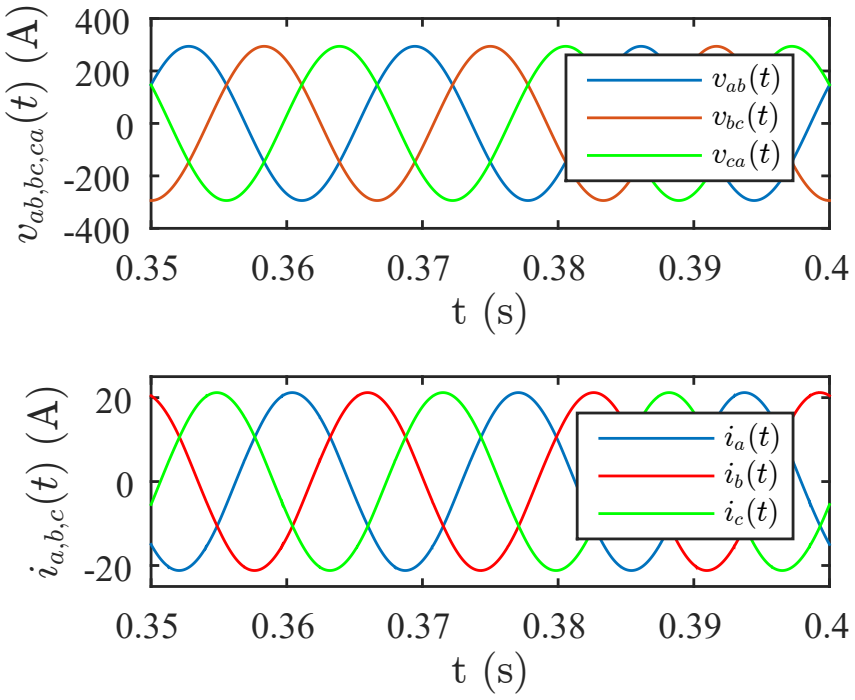

Figure 4.14: Simulation results: $v_{ab,bc,ca}(t)$ & $i_{a,b,c}(t)$ for (i_d, i_q) = (-15,-15) A

4.3 Simulation

The topology shown in Fig. 4.1 is modeled in PLECS using the parameters shown in Table 4.1. The matrix converter is operated such that $v_{ab}(t)$ is applied to the transformer for the first cycle of f_s, $v_{bc}(t)$ is applied to the transformer for the second cycle of f_s and $v_{ca}(t)$ is applied to the transformer for the third cycle of f_s. The half bridges are modulated using phase shifts $\phi_1^*(t)$ and $\phi_2^*(t)$ based on $i_d^*(t)$ and $i_q^*(t)$ input commands as shown in the control diagram Fig. 4.2. All the switches and diodes used in the simulation model are ideal. Fig. 4.3, Fig. 4.5, Fig. 4.7, Fig. 4.9, Fig. 4.11 and Fig. 4.13 depicts the source phase voltage $v_a(t)$ and source current $i_a(t)$ for phase A and Fig. 4.4, Fig. 4.6, Fig. 4.8, Fig. 4.10, Fig. 4.12 and Fig. 4.14 depicts the source line to line voltages $v_{ab}(t)$, $v_{bc}(t)$, $v_{ca}(t)$ and source currents $i_a(t)$, $i_b(t)$, $i_c(t)$ for (i_d, i_q) = (15,0), (-15,0), (15,15), (15,-15), (-15,15), (-15,-15). The simulation results confirm the converter ability to sink or source real and reactive into the AC grid.

CHAPTER 5

CONCLUSIONS AND FUTURE WORK

In the first chapter of this thesis, various types of electric vehicles have been discussed along with their advantages and disadvantages based on battery charging convenience and suitability of driving. Vehicle-to-grid (V2G) technology integration into the electric vehicle's on-board battery chargers has been discussed in detail. Literature review of the state of the art of on-board battery chargers reveals that the current charger topology is a two stage power conversion system and it also lacks bi-directional power flow capabilities.

This thesis focuses on three problem statements. Firstly, a single phase, single stage, isolated, bi-directional Silicon Carbide (SiC) AC-DC converter based on Dual Active Bridge (DAB) topology is proposed and analyzed. Secondly, a rigorous analysis is performed on the ripple rejection technique used in single phase bi-directional AC-DC converters. Finally, a three phase, single stage, isolated, bi-directional AC-DC converter is proposed and analyzed.

5.1 Single phase bi-directional SiC AC-DC converter

In the second chapter of this thesis, analysis of the modulation used for dual active bridge based single phase AC-DC converter was performed and a mathematical relationship between the average matrix converter current $i_m(t)$ and control variables $\delta^*(t)$ and $\phi^*(t)$ was derived. Hardware description and firmware computation timing are discussed in detail. Hardware results for active power transfer from the AC grid into the DC bus was shown confirming the simulation results and analytical predictions. Hardware results for other operating conditions can be obtained in future work.

5.2 DC ripple current rejection in a single phase bi-directional SiC AC-DC Converter

In the third chapter of this thesis, analysis of the ripple current rejection in a dual active bridge based AC-DC converter was discussed in detail. In order to cancel the ripple current, an additional half-bridge operating with a duty cycle d_c, was added in combination with an energy storage element. A mathematical expression for the duty cycle d_c was derived in terms of the control variables δ and ϕ_i. An average mathematical model for inverter leg currents $\bar{i}_{lega}$, $\bar{i}_{legb}$, and $\bar{i}_{legc}$ was developed to highlight the distinct unbalanced inverter leg currents. Simulation results were presented confirming the dc bus ripple current rejection with various operating conditions. Hardware results confirming the dc ripple rejection technique with DQ current control can be obtained in future work.

5.3 Three phase bi-directional SiC AC-DC converter

In the fourth chapter of this thesis, a brief analysis of the modulation technique used for a dual active bridge based three phase AC-DC converter is discussed. Mathematical relationships between the matrix converter currents $i_{md}(t)$, $i_{mq}(t)$, and control variables $\delta(t)$, $\phi(t)$ were derived. Simulation results were shown for various operating conditions confirming the analysis. Experimental results with sinking or sourcing real and reactive power including the THD analysis of the input current $i_a(t)$ and efficiency calculations can be obtained in future work.

BIBLIOGRAPHY

[1] "http://www.byd.com/na/auto/electricbus.html."

[2] M. Pahlevaninezhad, P. Das, J. Drobnik, P. Jain, and A. Bakhshai, "A zvs interleaved boost ac/dc converter used in plug-in electric vehicles," *Power Electronics, IEEE Transactions*, vol. 27, no. 8, pp. 3513 – 3529, Aug 2012.

[3] H. Wang, S. Dusmez, and A. Khaligh, "Design and analysis of a full-bridge llc-based pev charger optimized for wide battery voltage range," *Vehicular Technology, IEEE Transactions*, vol. 63, no. 4, pp. 1603 – 1613, May 2014.

[4] "Transportation electrification, utility fleets leading the charge," *Edison Electric Institue*, June 2014.

[5] H.-S. Kim, M.-H. Ryu, J.-W. Baek, and J.-H. Jung, "High-efficiency isolated bidirectional acdc converter for a dc distribution system," *Power Electronics, IEEE Transactions on*, vol. 28, no. 4, pp. 1642 – 1654, Apr 2014.

[6] K. Vangen, T. Melaa, and A. Adnanes, "Soft-switched high-frequency, high power dc/ac converter with igbt," *Power Electronics Specialists Conference*, vol. 1, pp. 26 – 33, 1992.

[7] N. Weise, K. Mohapatra, and N. Mohan, "Universal utility interface for plug-in hybrid electric vehicles with vehicle-to-grid functionality," in *Proc. IEEE Power and Energy Society General Meeting*, Jul. 2010, pp. 1–8.

[8] L. Doiron and N. Weise, "Dq current control of a bidirectional, isolated single-stage ac-dc converter," in *Applied Power Electronics Conference and Exposition (APEC), 2014 Twenty-Ninth Annual IEEE*, Mar. 2014, pp. 1888 – 1893.

[9] A. r. p. Andhra sridhar and N. Weise, "Implementation and validation of dq current control of a bidirectional sic single-phase ac-dc converter," in *Applied Power Electronics Conference and Exposition (APEC), 2015 IEEE*, March 2015, pp. 3143 – 3149.

[10] R. Wang, F. F. Wang, D. Boroyevich, R. Burgos, R. Lai, P. Ning, and K. Rajashekara, "A high power density single-phase pwm rectifier with active ripple energy storage," *Power Electronics, IEEE Transactions*, vol. 26, no. 5, pp. 1430 – 1443, Nov 2010.

[11] T. S. Y. Jin and G. Kimura, "Dc ripple current reduction on a single-phase pwm voltage-source rectifier," *Power Electronics, IEEE Transactions*, vol. 36,

no. 5, pp. 1419 – 1429, Oct 2000.

[12] N. Weise, K. Basu, and N. Mohan, "Advanced modulation strategy for a three-phase ac-dc dual active bridge for v2g," in *Proc. IEEE Vehicle Power and Propulsion Conference (VPPC'11)*, Sep. 2011, pp. 1–6.

[13] S. Brown, D. Pyke, and P. Steenhof, "Electric vehicles: The role and importance of standards in an emerging market," *Energy Policy*, vol. 38, no. 7, pp. 3797–3806, 2010.

[14] J. Tomi and W. Kempton, "Using fleets of electric-drive vehicles for grid support," *Journal of Power Sources*, vol. 168, no. 2, pp. 459–468, 2007. [Online]. Available: http://www.sciencedirect.com/science/article/pii/S0378775307005575

[15] S. Haghbin, S. Lundmark, M. Alaküla, and O. Carlson, "Grid-connected integrated battery chargers in vehicle applications: Review and new solution," *IEEE Trans. Ind. Electron.*,, vol. PP, no. 99, p. 1, 2012.

[16] B. Kramer, S. Chakraborty, and B. Kroposki, "A review of plug-in vehicles and vehicle-to-grid capability," in *Proc. IEEE Annual Conference of Industrial Electronics (IECON'08)*, Nov. 2008, pp. 2278–2283.

[17] M. El Chehaly, O. Saadeh, C. Martinez, and G. Joos, "Advantages and applications of vehicle to grid mode of operation in plug-in hybrid electric vehicles," in *Proc. IEEE Electrical Power Energy Conference (EPEC'09)*, Oct. 2009, pp. 1–6.

[18] M. Kisacikoglu, B. Ozpineci, and L. Tolbert, "Examination of a phev bidirectional charger system for v2g reactive power compensation," in *Proc. IEEE Applied Power Electronics Conference and Exposition (APEC'10)*, Feb. 2010, pp. 458–465.

[19] S. Haghbin, K. Khan, S. Lundmark, M. Alaküla, O. Carlson, M. Leksell, and O. Wallmark, "Integrated chargers for ev's and phev's: examples and new solutions," in *Proc. IEEE International Conference on Electrical Machines (ICEM'10)*, Sep. 2010, pp. 1–6.

[20] D. Erb, O. Onar, and A. Khaligh, "Bi-directional charging topologies for plug-in hybrid electric vehicles," in *Proc. IEEE Applied Power Electronics Conference and Exposition (APEC'10)*, Feb. 2010, pp. 2066–2072.

[21] G. Castelino, K. Basu, N. Weise, and N. Mohan, "A bi-directional, isolated, single-stage, dab-based ac-dc converter with open-loop power factor correction and other advanced features," in *Proc. IEEE International Conference on*

Industrial Technology (ICIT'12), Mar. 2012, pp. 938–943.

[22] N. Weise, "Dq current control of a bidirectional, isolated, single-stage ac-dc converter for vehicle-to-grid applications," in *Proc. IEEE Power and Energy Society General Meeting (PESGM'13)*, Jul. 2013.

[23] S. Safari, A. Castellazzi, and P. Wheeler, "Evaluation of sic power devices for a high power density matrix converter," in *Energy Conversion Congress and Exposition (ECCE)*, 2012, pp. pp. 3934 – 3941.

[24] Y. Sugawara, "Recent progress in sic power device developments and application studies," in *EEE 15th International Symposium on Power Semiconductor Devices and ICs*, 14-17 April 2003, pp. pp. 10–18.

[25] P. Friedrichs, "Silicon carbide power devices - status and upcoming challenges," in *Power Electronics and Applications, 2007 European Conference*, Sept. 2007, pp. pp. 1–11.

[26] T. Zhao, L. Yang, J. Wang, and A. Huang, "270 kva solid state transformer based on 10 kv sic power devices," in *Proc. IEEE Electric Ship Technologies Symposium (ESTS '07)*, May 2007, pp. 145–149.

[27] J. Gao, H. Sun, X. You, and T. Zheng, "A novel control strategy for current-source rectifiers with space vector modulation," in *Proc. IEEE Power Electronics Specialists Conference (PESC '08)*, Jun. 2008, pp. 3255–3258.

[28] J. Espinoza and G. Joos, "State variable decoupling and power flow control in pwm current source rectifiers," in *Proc. IEEE Industrial Electronics, Control, and Instrumentation, (IECON'95)*, vol. 1, Nov. 1995, pp. 686–691.

[29] N. Mohan, *Power Electronics: A First Course*. Wiley, 2012.

[30] N. Zargari, G. Joos, and P. Ziogas, "Input filter design for pwm current-source rectifiers," in *Proc. IEEE Applied Power Electronics Conference and Exposition (APEC'93)*, 1993, pp. 824–830.

[31] P. Wheeler and D. Grant, "Optimised input filter design and low-loss switching techniques for a practical matrix converter," *Proc. IEE Electric Power Applications*, vol. 144, no. 1, pp. 53–60, 1997.

[32] X. Wang, H. Lin, B. Feng, and Y. Lyu, "Damping of input lc filter resonance based on virtual resistor for matrix converter," in *Proc. IEEE Energy Conversion Congress and Exposition (ECCE'12)*, 2012, pp. 3910–3916.

[33] M. Allie and R. Lyons, "A root of less evil [digital signal processing]," *Signal Processing Magazine, IEEE*, pp. (Volume:22 , Issue: 2), Mar. 2005.

[34] S. Rajan, S. Wang, R. Inkol, and A. Joyal, "Efficient approximations for the arctangent function," *Signal Processing Magazine, IEEE (Volume:23 , Issue: 3)*, May 2006.

[35] N. D. Weise, G. Castelino, K. Basu, and N. Mohan, "A single-stage dual-active-bridge-based soft switched acdc converter with open-loop power factor correction and other advanced features," vol. 29, no. 8, Aug 2014.

[36] M. Yilmaz and P. T. Krein, "Review of battery charger topologies, charging power levels and infrastructure for plug-in electric and hybrid vehicles," vol. 28, no. 5, pp. 2151–2169, May 2013.

[37] M. C. K. Metin Kesler and L. M. Tolbert, "Vehicle-to-grid reactive power operation using plug-in electric vehicle bidirectional offboard charger," vol. 61, no. 21, Dec 2014.

[38] A. Lahyani, P. Venet, G. Grellet, and P.-J. Viverge, "Failure prediction of electrolytic capacitors during operation of a switch mode power supply," vol. 131, no. 6, pp. 1199–1206, Nov 1998.

[39] P. T. Krein and R. S. Balog, "Cost-effective hundred-year life for singlephase inverters and rectifiers in solar and led lighting applications based on minimum capacitance requirements and a ripple power port," in *Proc. IEEE Applied Power Electronics Conference and Exposition (APEC)*, 2009, pp. 620–625.

[40] D. Rendusara, E. Cingelci, P. Enjeti, and D. C. Lee, "An evaluation of the dc-link capacitor heating in adjustable speed drive systems with different utility interface options," in *Proc. IEEE Applied Power Electronics Conference and Exposition (APEC)*, 1999, pp. 781–787.

[41] M. L. Gasperi, "A method for predicting the expected life of bus capacitors," in *Proc. Industrial Applications Society Conference (IAS)*, vol. 2, 1997, pp. 1042–1047.

[42] J. L. Stevens, J. S. Shaffer, and J. T. Vandenham, "The service life of large aluminum electrolytic capacitors: effects of construction and application," vol. 3, pp. 2493–2499, 2001.